
DEEPSPOC: A DEEP LEARNING-BASED PDE SOLVER GOVERNED BY SEQUENTIAL PROPAGATION OF CHAOS

A PREPRINT

Kai Du *

Yongle Xie [†]

Tao Zhou [‡]

Yuancheng Zhou [§]

July 2024

ABSTRACT

Sequential propagation of chaos (SPoC) is a recently developed tool to solve mean-field stochastic differential equations and their related nonlinear Fokker-Planck equations. Based on the theory of SPoC, we present a new method (deepSPoC) that combines the interacting particle system of SPoC and deep learning. Under the framework of deepSPoC, two classes of frequently used deep models include fully connected neural networks and normalizing flows are considered. For high-dimensional problems, spatial adaptive method are designed to further improve the accuracy and efficiency of deepSPoC. We analysis the convergence of the framework of deepSPoC under some simplified conditions and also provide a posterior error estimation for the algorithm. Finally, we test our methods on a wide range of different types of mean-field equations.

1 Introduction

A wide range of nonlinear partial differential equations (PDEs) in kinetic theory can be associated with the so-called mean-field stochastic differential equations (SDEs), which can be expressed in the following general form:

$$dX_t = b(t, X_{t-}, \mu_t)dt + \sigma(t, X_{t-}, \mu_t)dZ_t, \quad (1)$$

where μ_t denotes the distribution of X_t , and Z_t is a multidimensional Lévy process, including Poisson and compound Poisson process, Brownian motion and other stable processes as its special case. The distribution of the solution of the mean-field SDE μ_t is a weak solution of its related nonlinear PDE in the distributional sense. These nonlinear PDEs, commonly referred to as nonlinear Fokker-Planck equations, describe the time evolution of the probability distribution of particles under the influence of external forces (including random noise). These PDEs have important applications in fluid dynamics, biology, chemistry and other fields (see the review paper [1]). However, most of them are difficult to solve numerically due to their non-linearity caused by the mean-field term and some other unfavorable properties. The relation between the PDEs and SDEs inspires us to solve the problem from the perspective of the related SDEs. To solve mean-field SDEs, the propagation of chaos theory (PoC for short) [2, 3] demonstrates that a wide range of these mean-field SDEs can be viewed as the mean-field limit equations of an interacting particle system. Hence their solutions can be approximated by the empirical measure of the particles of the system. This insight has led to the development of various particle methods, including deterministic particle methods [4, 5] and stochastic particle methods [6, 7, 8, 9] and some related calculation techniques like random batch method [10]. These methods aim at providing numerical solutions for mean-field SDEs and consequently resolving their associated PDEs concurrently.

Compared with traditional methods such as finite difference or finite element method, particle methods have various advantages. Particle methods are mesh-free, hence are more flexible with respect to space dimensions, while the

*Shanghai Center for Mathematical Sciences, Fudan University, Shanghai, 200438, China. Email: kdu@fudan.edu.cn

[†]Shanghai Center for Mathematical Sciences, Fudan University, Shanghai, 200433, China. Email: 24110840016@m.fudan.edu.cn

[‡]LSEC, Institute of Computational Mathematics and Scientific/Engineering Computing, AMSS, Chinese Academy of Sciences, Beijing, China. Email: tzhou@lsec.cc.ac.cn.

[§]LSEC, Institute of Computational Mathematics and Scientific/Engineering Computing, AMSS, Chinese Academy of Sciences, Beijing, China. Email: yzhou@lsec.cc.ac.cn.

increase in dimensions can bring an unbearable computational burden for traditional mesh-based methods. In addition, the nonlinear mean-field terms of the equations together with the possibly non-local operator brought by Lévy process also make it difficult to apply traditional methods.

However, these widely used particle methods also have some shortcomings. First, these methods require simulation of a large number of particles (i.e. numerically solving a large system of stochastic or ordinary differential equations representing the interacting particles) which results in huge computational costs. Second, constructing the solution solved by particle methods requires to store trajectories of all particles, which leads to massive computational storage requirement. The two aforementioned difficulties become more prominent when solving high-dimensional problems because they need to simulate and store more particles to ensure accuracy.

Recently, there has been a growing interest in using deep learning techniques to solve PDEs. Deep learning methods such as physics-informed neural networks (PINNs) [11], Deep Ritz method [12] and weak adversarial networks (WANs) [13], Deep BSDE [14] have been successfully applied to address various PDE related problems. These deep learning approaches have many advantages. First, they are potential numerical methods to solve high-dimensional problems since they are mesh-free. Second, they can fully utilize the computing resources of GPUs. However, despite deep learning methods showing many advantages when solving PDEs, they can still encounter some difficulties when addressing PDEs with non-linearity and non-local terms. Given the strength of particle methods in handling mean-field equations, a natural question arises: Can we combine particle methods with neural network methods while avoiding their individual shortcomings?

In this paper, we develop a neural networks based sequential particle method to solve the mean-field SDEs (1) which can avoid the two shortcomings of particle methods mentioned above. In our method, the specific forms of how b and σ depend on the distribution μ_t can be very diverse, including density dependent type (e.g., porous medium equations, fractional porous medium equations) and distribution dependent type (e.g., Keller-Segel equations, Curie-Weiss mean-field equations), see Section 4 for the applications of our method to various forms of mean-field equations. Building upon ideas and theoretical foundations drawn from the recent paper on sequential propagation of chaos [15] (SPoC), our approach which we refer to as deepSPoC is to use a neural network to fit the empirical distribution of particles rather than directly store all the position of particles. This allows us to avoid the storage of a large number of particle trajectories. More specifically, we use a neural network that involves continuous time and space as inputs to fit the density function (or distribution) of the simulated particles over a period of time. Thanks to the sequential structure of SPoC, we can simulate particles in batches rather than simulate all particles at the same time. Therefore the algorithm based on SPoC has an iterative form which is suitable for deep learning. By constructing appropriate loss function, the neural network can learn and assimilate information from the newly simulated particle batch and gradually converges to the desired mean-field limit of the interacting particle system. The main contributions of our method can be summarized as follows:

- By using neural network to parameterize the position of particles, we can avoid storing trajectory of particles, hence save memory space significantly.
- This method inherits the recursive form of SPoC algorithm, so that we don't need to simulate all particles at one time like other particle methods. This alleviates the computational cost of simulating a large number of particles simultaneously and also makes the algorithm more flexible when the number of particles changes due to different accuracy requirements.
- As a mesh-free neural network based method, this approach can be applied to solve equations in higher space dimensions comparing with traditional methods. In addition, the simulated particles path data in the algorithm can lead to natural and convenient adaptive strategy for choosing training set when dealing with high-dimensional problems.
- In most cases, deepSPoC does not require differentiation to neural networks or at least reduces the order of differentiation, which avoids the huge computational burden caused by automatic differentiation for high-order derivatives. Furthermore, it reduces the requirement for smoothness of neural networks, which allows us to use wider range of neural network structures to fit the solution.

The remainder of this paper is structured as follows. In Section 2, we introduce the background theory of deepSPoC, along with its specific implementation and underlying motivation. Section 3 is some theoretical analysis about deepSPoC algorithm, including a convergence analysis and a posterior error estimation of the algorithm under some simplified assumptions. In Section 4 we show the numerical results of the deepSPoC algorithm applied to various types of equations.

2 DeepSPoC algorithm

2.1 Background and a sketch of deepSPoC

In this subsection we discuss the basic ideas of PoC and SPoC, then we explain how the deepSPoC algorithm is formulated as a generalization and extension of these two methods.

First, the nonlinear Fokker-Planck equations associated to SDEs (1) are as follows:

$$\partial_t \mu_t(x) = \mathcal{L}^*(t, \mu_t)(\mu_t(x)), \quad (2)$$

where μ_t is the distribution of random variable X_t in (1) and the nonlinear operator $\mathcal{L}^*(t, \mu_t)$, which dependents on both t and μ_t , is from the drift term and the diffusion term driven by Lévy process Z_t in (1). For example, if we choose the Lévy process Z_t to be a Brownian motion B_t , then the SDE will become a McKean-Vlasov type and the PDE will have the following form:

$$\partial_t \mu_t(x) = -\nabla_x \cdot (b(t, x, \mu_t)\mu_t(x)) + \frac{1}{2} \sum_{i,j=1}^d \partial_{x_i} \partial_{x_j} (a_{ij}(t, x, \mu_t)\mu_t(x)), \quad (3)$$

which is a second order Fokker-Planck equation. The diffusion coefficient $a(t, x, \mu) := \sigma(t, x, \mu)\sigma(t, x, \mu)^T$ and d is the dimension of X_t . In order to derive that μ_t of (1) is a weak solution of PDE (2), we can choose a test function ϕ and apply Itô's formula to $\phi(X_t)$, then we can get the weak form of the nonlinear evolution equation (2). For the general Itô's formula when SDE is driven by Lévy process and the explicit form of the operator $\mathcal{L}^*(t, \mu_t)$ (which is the adjoint operator of the infinitesimal generator associated with the process (1)), we refer the reader to [16].

Since we have such connection between a nonlinear PDE and a mean-field SDEs, the solution of the PDE can be solved by calculating the SDE. Note that the mean-field SDE can not be simulated directly by Monte Carlo method since it has mean-field terms and, therefore, not Markovian. The famous propagation of chaos (PoC) theory suggests the construction of an interacting particle system to approximate the mean-field SDE. The interacting particle system with N particles $\{X^{n,N} : n = 1, 2, \dots, N\}$ usually takes the form

$$\begin{cases} dX_t^{n,N} = b(t, X_{t-}^{n,N}, \mu_t^N)dt + \sigma(t, X_{t-}^{n,N}, \mu_t^N)dZ_t^n \\ \mu_t^N = \frac{1}{N} \sum_{i=1}^N \delta_{X_t^{i,N}}. \end{cases} \quad (4)$$

where Z^n are independent multidimensional Lévy processes and the initial data $X_0^{n,N} \sim \mu_0$ are i.i.d. \mathbb{R}^d -valued random variables. In general, the PoC theory demonstrates that for a variety of different types of the mean-field SDE (1) (including some singular kernel interaction cases, see e.g., [17, 18] and the review paper [19]), if the particle number N of the interacting particle system tends to infinity, the empirical measure of particles μ_t^N will converge to the distribution μ_t in (1) in a certain sense. A special case is that when dealing with density dependent mean-field SDE, the empirical measure μ_t^N in the above interacting particle system can be replaced by the density function $\rho_t^N = \mu_t^N * f_\epsilon$, which is the mollified empirical measure, where f_ϵ is the mollifier and in this paper, it is often chosen as the Gaussian mollifier:

$$f_\epsilon(x) = \frac{1}{(2\pi\epsilon^2)^{\frac{d}{2}}} e^{-\frac{|x|^2}{2\epsilon^2}}. \quad (5)$$

An example for the density dependent mean-field SDE is porous medium equation and its PoC result for mollified particle system can be found in [20].

Unlike the classical interacting particle system (4), SPoC theory provides a different way for particles to interact: each particle only needs to interact with the preceding ones. Therefore, the system has an iterative form, allowing more and more particles to be added progressively. The interacting particle system $\{X^n\}_{\{n \geq 1\}}$ of SPoC takes the form

$$\begin{cases} dX_t^n = b(t, X_{t-}^n, \mu_t^{n-1})dt + \sigma(t, X_{t-}^n, \mu_t^{n-1})dZ_t^n \\ \mu_t^n = \mu_t^{n-1} + \alpha_n (\delta_{X_t^n} - \mu_t^{n-1}), \end{cases} \quad (6)$$

where μ_t^0 can be chosen as any initial guess of the distribution, α_n denotes the update rate, which is usually decreasing and converge to 0 as $n \rightarrow \infty$, and $X_0^n \sim \mu_0$ are i.i.d. \mathbb{R}^d -valued random variables. In [15], it is proved that for McKean-Vlasov diffusion (when Z_t is a Brownian motion), if the drift function b and the diffusion matrix σ satisfy the monotonicity condition, and the update rate α_n is selected appropriately, then μ_t^n will converge to μ_t of the mean-field SDE(1) according to Wasserstein distance as $n \rightarrow \infty$.

System (6) is a particle by particle system, a batch by batch version of SPoC is also introduced in [15], where the n -th batch contains K particles $\{X^{i,n} : i = 1, \dots, K\}$ and by $\hat{\mu}^n$ we denote the empirical measure of the trajectories of this n -th batch particles, i.e.,

$$\hat{\mu}^n := \frac{1}{K} \sum_{i=1}^K \delta_{X^{i,n}}, \quad (7)$$

and naturally, we denote the time marginal of $\hat{\mu}^n$ by

$$\hat{\mu}_t^n := \frac{1}{K} \sum_{i=1}^K \delta_{X_t^{i,n}},$$

then the interacting particle system for batch by batch SPoC is constructed as

$$\begin{cases} dX_t^{i,n} = b(t, X_{t-}^{i,n}, \mu_t^{n-1}) dt + \sigma(t, X_{t-}^{i,n}, \mu_t^{n-1}) dZ_t^{i,n}, i = 1, \dots, K \\ \mu_t^n = \mu_t^{n-1} + \alpha_n (\hat{\mu}_t^n - \mu_t^{n-1}), \end{cases} \quad (8)$$

with the initial data $X_0^{i,n} \sim \mu_0$ still i.i.d. random variables. This batch by batch form is usually more efficient in practice because it allows a batch of particles to be merged into a single tensor for parallel computation.

Now we begin to introduce the deepSPoC algorithm, and we can see how it is designed based on SPoC. As a numerical algorithm, deepSPoC exploits the iterative form of SPoC to become a deep learning algorithm. The interacting particle system belongs to deepSPoC is

$$\begin{cases} dX_t^{i,n} = b(t, X_{t-}^{i,n}, \rho_{NN, \theta_{n-1}}(t, \cdot)) dt + \sigma(t, X_{t-}^{i,n}, \rho_{NN, \theta_{n-1}}(t, \cdot)) dZ_t^{i,n}, i = 1, \dots, K \\ \rho_{NN, \theta_n} = F(\rho_{NN, \theta_{n-1}}, \hat{\mu}^n, \alpha_n), \end{cases} \quad (9)$$

where $\rho_{NN, \theta_{n-1}} (n \geq 1)$ is a neural network (ρ_{NN, θ_0} is the initialized neural network) that for fixed t , $\rho_{NN, \theta_{n-1}}(t, \cdot) : \mathbb{R}^d \rightarrow \mathbb{R}$ tries to fit a density function that is approximate to the weighted empirical distribution formed by all simulated particles like μ_t^{n-1} in (8). The most important part of the system is the operator F , which represents the method of how to update the neural network. More specifically, when given the current neural network $\rho_{NN, \theta_{n-1}}$, empirical measure of newly simulated particle batch $\hat{\mu}^n$ and the update rate α_n , the operator F will update the current neural network's parameter θ_{n-1} to θ_n and therefore give the updated neural network ρ_{NN, θ_n} . The complete definition of F includes the construction of a loss function, the computation of gradient according to this loss function, and the execution of one gradient descent step on the parameters by an optimizer. We will explain these in detail in the next subsection.

Comparing deepSPoC's system (9) with SPoC's system (8), in order to achieve that as $n \rightarrow \infty$, $\rho_{NN, \theta_n}(t, \cdot)$ converges to the density of μ_t in (1), the design of the deepSPoC algorithm needs to meet the following two requirements:

- The neural network we choose have the ability to approximate the empirical measure formed by simulated particles in a period of time.
- The parameter update method F can make the neural network absorb the information from newly simulated particles. For example, it can roughly achieve the effect of a weighted average, where the weights depend on α_n , similar to how μ_t^n is updated in (8).

While the theory of PoC and SPoC and the structure of their particle systems are the foundations of our deepSPoC algorithm, it should be acknowledged that the general equation (1) and many of the specific equations we compute in our numerical experiments actually go beyond the scope of the SPoC theory or even PoC theory, especially for the cases of singular interaction kernels and the equation which is driven by general Lévy process. However we hope that the background theory we mention in this subsection can partially and intuitively explain why the deepSPoC algorithm can performs well in a broad range of equations.

Remark 1. Note that the system (9) can be applied to both density dependent case and distribution dependent case, while for PoC and SPoC's particle systems (4)(6)(8) we need to perform additional mollification on the empirical measure of particles when dealing with density dependent case. Actually, it can be found in the next subsection that the mollification of empirical measure is included in the definition of F , and also implicitly included in the action of fitting time-dependent density functions by neural networks.

2.2 Detailed implementation of deepSPoC algorithm

The whole algorithm is based on the deepSPoC's interacting particle system (9). According to (9), in the n -th iteration, we need to simulate a batch of particles by substituting the neural network into the SDE, then applying the operator F to update the neural network; we refer to this entire process as an epoch of deepSPoC. Now we explain the detailed process of a complete epoch of deepSPoC in practice.

Assume the current neural network is $\rho_{NN,\theta}$. First we substitute the current neural network $\rho_{NN,\theta}$ into the SDE (9) and use Euler-Maruyama scheme to numerically solve it. We equally divide the total time interval $[0, T]$ into M subintervals, i.e., $0 = t_0 < t_1 < \dots < t_M = T$, the time step size is $\Delta t = T/M$, then simulate a batch of particles $\{X^i : i = 1, \dots, K\}$ as follows (for the convergence results of Euler scheme for Lévy driven SDEs, readers can refer to [21]):

$$X_{t_m}^i - X_{t_{m-1}}^i = b(t_{m-1}, X_{t_{m-1}}^i, \rho_{NN,\theta}(t_{m-1}, \cdot)) \Delta t + \sigma(t_{m-1}, X_{t_{m-1}}^i, \rho_{NN,\theta}(t_{m-1}, \cdot)) \Delta Z_t^i, \quad (10)$$

with the initial points $\{X_0^i\}_{\{i=1, \dots, K\}}$ i.i.d. sampled from the initial distribution μ_0 . Then we get the empirical measure of the particles at each discrete time point, i.e.,

$$\hat{\mu}_{t_m} = \frac{1}{K} \sum_{i=1}^K \delta_{X_{t_m}^i}, \quad m = 0, \dots, M,$$

which can be seen as the discrete version of $\hat{\mu} = (1/K) \sum_{i=1}^K \delta_{X^i}$.

Second we use this empirical measure to update the parameters of the current neural network, which is the most important part of deepSPoC algorithm. When the update rate $\alpha > 0$ is chosen, the implementation of the update method (which can be seen as the discretized version of operator F) can be divided into three steps:

- Step1 Construct a loss function $L(\rho_{NN,\theta}, \{\hat{\mu}_{t_m}\}_{\{m=0, \dots, M\}})$ which can be calculated by the current neural network and the empirical measure of particles.
- Step2 Compute the gradient of the loss function with respect to the neural network's parameters, that is, compute $\nabla_{\theta} L(\rho_{NN,\theta}, \{\hat{\mu}_{t_m}\}_{\{m=0, \dots, M\}})$.
- Step3 Execute one gradient descent step on the neural network parameters by an optimizer (such as the Adam optimizer) with the learning rate α .

Then we finish a complete epoch of the deepSPoC algorithm. A general framework of deepSPoC is shown in Fig 1.

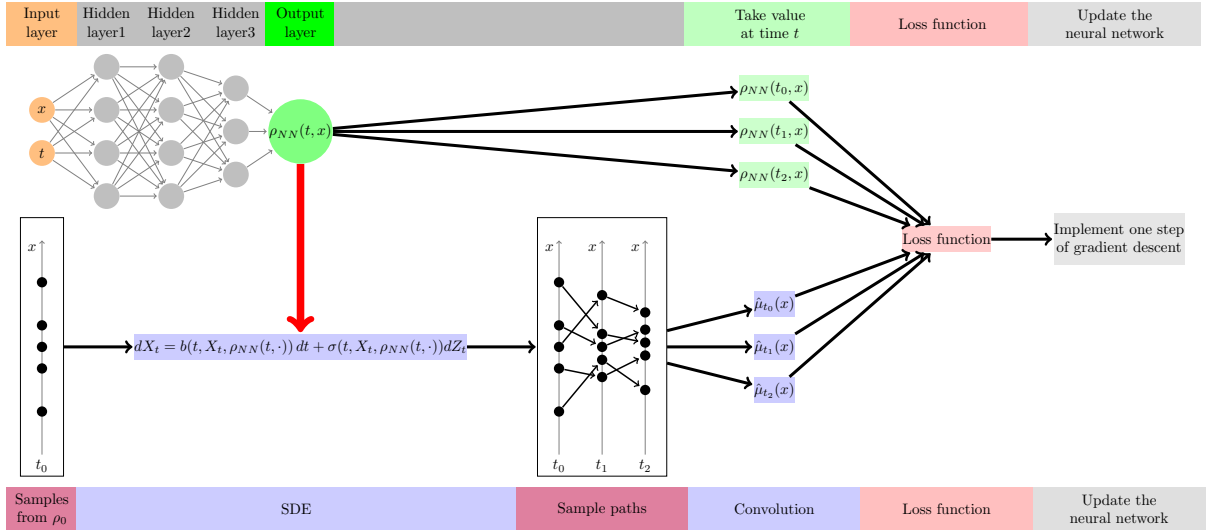


Figure 1: The flow chart of the deepSPoC

Here are some further discussions on the loss function L . We point out that the role of the loss function in deepSPoC is very different from its role in many classical deep learning algorithms. The entire algorithm is not solving an

optimization problem like a typical machine learning task. Therefore referring to L as the loss function might be somewhat misleading because we do not intend to minimize it during the training process. In fact, since the distribution of the simulated particles changes with epochs, the loss function L with respect to θ also changes with epochs. We use gradient descent as a method to help our neural network assimilate the information from the newly simulated particles (for example, approximating the effect of weighted average of empirical measures) rather than minimizing the current loss function. That is also why we only execute one gradient descent during each epoch.

Now the question is what the explicit form of the function L is. We have tried different forms of L and sometimes the choice of L also depends on the type of neural network we use. In the following subsections, we introduce the two types of neural networks with their corresponding loss functions that we have tried in our numerical experiments.

2.2.1 DeepSPoC with fully connected neural networks

We first consider the $\rho_{NN,\theta}$ to be a fully connected neural network. The fully connected neural network $\rho_{FC,\theta} : \mathbb{R}^{d+1} \rightarrow \mathbb{R}$ with m hidden layers has the following well-known structure:

$$\rho_{FC,\theta}(t, x) = L_m \circ R \circ L_{m-1} \circ \dots \circ R \circ L_0(t, x),$$

where $x \in \mathbb{R}^d$ is space variable and $t \in \mathbb{R}$ is time variable, $\{L_i\}_{i=0,\dots,m}$ are linear transformations and R is the activation function which is typically chosen as ReLU in our experiments.

By $\hat{\rho}_{t_m}$ we denote the mollified empirical measure $\hat{\mu}_{t_m} * f_\epsilon$. Recall that f_ϵ is the Gaussian mollifier we have defined in (5), and the mollification scale ϵ should be determined in advance, which depends on the accuracy requirement of the numerical solution. The first loss function we construct which is denoted by L_{sq} has the following L^2 -distance form:

$$L_{\text{sq}}(\rho_{FC,\theta}, \{\hat{\mu}_{t_m}\}_{m=0,\dots,M}) = \sum_{m=0}^M \|\rho_{FC,\theta}(t_m, \cdot) - \hat{\rho}_{t_m}(\cdot)\|_{L^2}^2. \quad (11)$$

To estimate this L^2 -distance, for every epoch, we select N training points uniformly from a pre-determined truncated region $\Omega_0 \subset \mathbb{R}^d$ to form a training set $S = \{x^j\}_{j=1,\dots,N}$. The bounded region Ω_0 is pre-determined by our prior knowledge and estimation of the solution. For simplicity of our notation, we assume the constant of the volume of $|\Omega_0|$ is 1 throughout this section. In fact, in experiments where it is necessary to estimate the loss function, we usually ignore this constant, as it does not have any big impact on the results. Using the training set S , we can estimate the above L_{sq} as follows:

$$\begin{aligned} L_{\text{sq}}(\rho_{FC,\theta}, \{\hat{\mu}_{t_m}\}_{m=0,\dots,M}) &\approx \sum_{m=0}^M \frac{1}{N} \sum_{x \in S} |\rho_{FC,\theta}(t_m, x) - \hat{\rho}_{t_m}(x)|^2 \\ &= \frac{1}{N} \sum_{m=0}^M \sum_{x \in S} \left| \rho_{FC,\theta}(t_m, x) - \frac{1}{K} \sum_{i=1}^K \frac{1}{(2\pi\epsilon^2)^{\frac{d}{2}}} e^{-\frac{|x-x_{t_m}^i|^2}{2\epsilon^2}} \right|^2. \end{aligned} \quad (12)$$

In practice, we take the derivative of the right-hand side of the above equation to approximate the gradient of the loss function L_{sq} with respect to θ .

A large part of our numerical results (see in section 4) are based on this L^2 -distance function L_{sq} together with fully connected neural networks. A natural problem for the fully connected neural network is that it is not a strict probability density function at each time point. To compensate for this drawback of fully connected networks, we need to carefully select the loss function. Specifically, we find that together with this appropriate L_{sq} , the fully connected neural network can gradually acquire the property of probability density function during the training process, and perform well in solving various types of mean-field equations.

Remark 2. When calculating the gradient, we view $\hat{\rho}_{t_m}(x^j) = (\hat{\mu}_{t_m} * f_\epsilon)(x^j)$ as a constant which is independent of θ , though it actually depends on the neural network during the simulation (10). Therefore during the experiment, the back propagation of gradient is detached for the process of simulating particles.

Remark 3. The loss function L_{sq} can be further divided by the time discrete steps $M + 1$, which makes the update process more reasonable to be a discretized version of operator F . However, the experimental results do not have significant difference whether divide this constant or not. In addition, when using optimizers like Adam optimizer, the update of the parameter also depends on the previous gradients, so the expression $\rho_{FC,\theta_n} = F(\rho_{FC,\theta_{n-1}}, \hat{\mu}^n, \alpha_n)$ in (9) is actually not entirely rigorous.

2.2.2 DeepSPoC with normalizing flows

Instead of applying a fully connected neural network, we use a temporal normalizing flow [22, 23] $\rho_{NF,\theta}(t, \cdot)$ with θ as unknown parameter to approximate the time-dependent density function ρ_t in this section. Normalizing flows [24, 25] are a class of generative models that construct complex probability distributions by transforming a simple initial distribution (like a Gaussian) through a series of invertible and differentiable mappings. A temporal normalizing flow is a time dependent generative model which at any fixed time t in temporal domain, it is a normalising flow. Unlike the fully connected neural network, for fixed $t \in [0, T]$, the normalizing flow $\rho_{NF,\theta}(t, \cdot)$ as a density function automatically satisfies the following two rules

- Nonnegativity, i.e., $\rho_{NF,\theta}(t, x) \geq 0, \forall x \in \mathbb{R}^d$;
- Its integral equals to one, i.e., $\int \rho_{NF,\theta}(t, x) dx = 1$.

When a fully connected neural network is used to approximate the density function, these two rules can be violated. Another advantage of using temporal normalizing flow is we can draw new samples from it directly while we have to use accept-reject sampling in fully connected neural network case. This direct sampling feature can significantly improve efficiency when numerically solving the SDE as in (10) which b (or σ) involves integrals with respect to the density function.

In particular, we use a recently developed normalizing flow called KRnet [26] to build temporal generative model. For the implementation of temporal KRnet to deepSPoC, we can also use the L^2 -distance loss function L_{sq} defined in (11). Moreover, another significant advantage of using normalizing flows is that we can use more probabilistic loss functions because of their inherent property to be a probability density function. For example, instead of comparing the L^2 -distance between $\hat{\rho}_{t_m}$ and $\rho_{NF,\theta}(t_m, \cdot)$, we can also construct the following loss function:

$$\sum_{m=0}^M D_{\text{KL}}(\hat{\rho}_{t_m} \parallel \rho_{NF,\theta}(t_m, \cdot)), \quad (13)$$

where the KL-divergence from $\hat{\rho}_{t_m}$ to $\rho_{NF,\theta}(t_m, \cdot)$ is defined as

$$D_{\text{KL}}(\hat{\rho}_{t_m} \parallel \rho_{NF,\theta}(t_m, \cdot)) = \int_{\mathbb{R}^d} \hat{\rho}_{t_m}(x) \log(\hat{\rho}_{t_m}(x)) dx - \int_{\mathbb{R}^d} \hat{\rho}_{t_m}(x) \log(\rho_{NF,\theta}(t_m, x)) dx. \quad (14)$$

Since the first term in (14) is not a function of the parameter θ , we only need to calculate the second term at different time steps and add them together:

$$L_{\text{kl}}(\rho_{NF,\theta}, \{\hat{\rho}_{t_m}\}_{m=0, \dots, M}) = - \sum_{m=0}^M \int_{\mathbb{R}^d} \hat{\rho}_{t_m}(x) \log(\rho_{NF,\theta}(t_m, x)) dx. \quad (15)$$

Suppose the training set $S = \{x^j\}_{j=1, \dots, N}$ is sampled from the uniform distribution on $\Omega_0 \subset \mathbb{R}^n$, then L_{kl} can be estimated as follows:

$$L_{\text{kl}}(\rho_{NF,\theta}, \{\hat{\rho}_{t_m}\}_{m=0, \dots, M}) \approx - \sum_{m=0}^M \frac{1}{N} \sum_{x \in S} \hat{\rho}_{t_m}(x) \log(\rho_{NF,\theta}(t_m, x)). \quad (16)$$

Again we use the gradient of the right-hand side of the above equation with respect to θ to approximate the gradient of the loss function L_{kl} with respect to θ .

Another natural way to build loss function is constructing it as a negative logarithm likelihood function:

$$\begin{aligned} L_{\text{path}}(\rho_{NF,\theta}, \{\hat{\rho}_{t_m}\}_{m=0, \dots, M}) &= - \sum_{m=0}^M \int \log(\rho_{NF,\theta}(t_m, x)) \hat{\rho}_{t_m}(dx) \\ &= - \sum_{m=0}^M \frac{1}{K} \sum_{i=1}^K \log(\rho_{NF,\theta}(t_m, X_{t_m}^i)). \end{aligned} \quad (17)$$

For this loss function, we do not need to sample training points to estimate it. More importantly, it does not require mollifying the empirical measure $\hat{\rho}_{t_m}$. Therefore using this loss function can reduce the computational cost and it is also more suitable to deal with high-dimensional problems because of its mollification free form. This loss function is also used to develop deep solvers for other types of SDEs [27].

Remark 4. In particular, if the training sets $S_m = \{x_m^j\}_{\{j=1, \dots, N\}}$ in the (15) are sampled from the density function $\hat{\rho}_{t_m}$, then L_{kl} can be estimated as

$$L_{kl}(\rho_{NF, \theta}, \{\hat{\mu}_{t_m}\}_{\{m=0, \dots, M\}}) \approx - \sum_{m=0}^M \frac{1}{N} \sum_{x \in S_m} \log(\rho_{NF, \theta}(t_m, x)). \quad (18)$$

A straightforward training set which can be used in (18) is formed by the sampled particles $\{X_{t_m}^i\}$ at each time t_m (ignoring the bias caused by mollification). In this case, (18) can be written as

$$L_{kl}(\rho_{NF, \theta}, \{\hat{\mu}_{t_m}\}_{\{m=0, \dots, M\}}) \approx - \sum_{m=0}^M \frac{1}{K} \sum_{i=1}^K \log(\rho_{NF, \theta}(t_m, X_{t_m}^i)). \quad (19)$$

Comparing (19) with (17), we can see that the value of L_{kl} is actually close to L_{path} .

2.2.3 The choose of update rate and the convergence of the algorithm

We have already discussed some special aspects of the deepSPoC algorithm compared to other deep learning algorithms, one major difference is the different roles of the loss function in these algorithms. For many other deep learning algorithms, the value of the loss function becoming stable and no longer decreasing is a signal of convergence. However, things are different when considering deepSPoC's convergence, because our object is not minimizing the loss function. In fact, in our numerical experiments, we observe that the value of loss function fluctuates around a certain level for most of time after a rapid descent at the beginning. Fig. 2 shows this phenomenon when solving the 1D porous medium equation using fully connect neural network, where the orange line is the L^2 -distance loss function changes with epochs, and the blue line is the relative L^2 error between the deepSPoC's numerical solution and the real solution. We can see that although the numerical solution is becoming increasingly accurate, the loss value has not changed significantly.

Recall that for the interacting particle system of SPoC (8), μ_t^n converges when the update rate α_n converges to zero with a certain rate. However the update rate cannot decrease to 0 too fast in order to obtain the enough information from particles. For deepSPoC, we view the learning rate we set for the optimizer in each epoch plays the similar role as α_n in (8). Since α_n controls the convergence of the SPoC, the learning rate for each epoch (we also denote it by α_n) should also be important for deepSPoC to ensure that the algorithm converges and converges to a good result. In practice, we find that reducing the learning rate by a contraction factor $\gamma < 1$ for every certain number of epochs (denoted by Γ) can strikes a balance between convergence speed and convergence results, i.e., for $n \geq 1$, set

$$\alpha_n = \alpha_0 \gamma^{\lfloor \frac{n}{\Gamma} \rfloor},$$

- where $\lfloor x \rfloor$ represents rounding down of x .

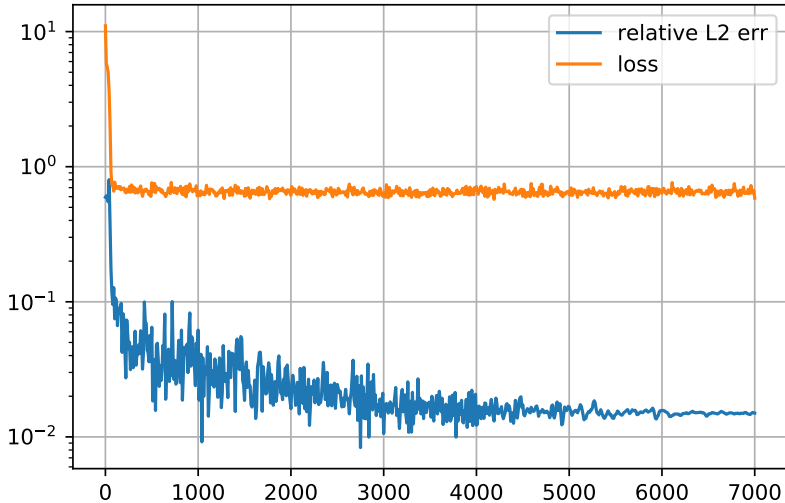


Figure 2: Loss v.s. relative L^2 error in the 1D porous medium equation.

However, it should be admitted that although we can ensure the convergence of deepSPoC by setting appropriate update rate α_n , we do not know how far the result is from the true solution during the training process. Some theoretical posterior error estimation analysis is given in Section 3.2. More general and convenient forms of posterior estimation of the error between the numerical solution and true solution will be our future work.

2.2.4 Adaptive sampling strategy

In the previous section, for the case that we need to choose a training set S in each epoch to estimate the loss function (e.g. L_{sq}), S is uniformly sampled from a truncated region Ω_0 . According to our experimental results, this uniform sample method for estimating L_{sq} is effective for low-dimensional problems with a spatial dimension of 1 or 2. However, when dealing with higher-dimensional problems, we find that choosing training set uniformly is inefficient, because the main support of the solution (i.e., the region that contains most of the probability for the density function) only takes a low proportion of the total volume of Ω_0 for high-dimensional problems, and most of the training points x^j contribute very little to the loss function. Therefore we need some adaptive strategy for updating our training set S in high-dimensional problems.

Fortunately, the algorithm itself provides convenient and natural adaptive method. We can use the simulated particles in the last epoch with an additional noise as part of our training set, so that our training points can be more concentrated in the region that containing more information about the density function. For this adaptive strategy, the training set at t_m which is denoted by S_m consists of two parts

$$S_m = S_{\text{uniform}} \cup S_{\text{adaptive}}^m,$$

where the training points in $S_{\text{uniform}} = \{x^j\}_{\{j=1, \dots, N_1\}}$ is uniformly selected in the area Ω_0 like before, and S_{adaptive}^m is defined as follows:

$$S_{\text{adaptive}}^m = \left\{ x^j \mid x^j = \hat{X}_{t_m}^j + \sigma \delta_j, j = 1, \dots, N_2 \right\}$$

where $\hat{X}_{t_m}^j$ is randomly selected from sampled particles at t_m in the last epoch, here we assume $N_2 \leq K$ where K is the batch size of sampled particles (if it is the first epoch, then $\hat{X}_{t_m}^j$ is just randomly sampled from the given initial distribution or simply set $S_{\text{adaptive}}^m = \emptyset$), and $\{\delta_j\}_{\{j=1, \dots, N_2\}}$ are i.i.d. sampled noise from standard Gaussian distribution $\mathcal{N}(0, 1)$, the parameter $\sigma \geq 0$ controls the intensity of the noise. The purpose of adding the noise is to make our adaptive training set retain the ability of “exploration”. We use this new training set to estimate the loss function. For example, the adaptive version of L^2 -distance loss function is

$$\begin{aligned} L_{\text{adaptive}}(\rho_{FC, \theta}, \{\hat{\mu}_{t_m}\}_{\{m=0, \dots, M\}}) &= \sum_{m=0}^M \frac{1}{N_1 + N_2} \sum_{x \in S_m} |\rho_{FC, \theta}(t_m, x) - (\hat{\mu}_{t_m} * f_\epsilon)(x)|^2 \\ &= \frac{1}{N_1 + N_2} \sum_{m=0}^M \sum_{x \in S_m} \left| \rho_{FC, \theta}(t_m, x) - \frac{1}{K} \sum_{i=1}^K \frac{1}{(2\pi\epsilon^2)^{\frac{d}{2}}} e^{-\frac{|x - \hat{X}_{t_m}^i|^2}{2\epsilon^2}} \right|^2. \end{aligned} \quad (20)$$

The adaptive sampling strategy for deepSPoC with KL divergence loss is different from that for the L^2 -distance loss. Adding new non-uniform sampled training points to the original uniform training set S_{uniform} can change the computing measure of the integrals in the L_{kl} . In this case, the estimation is not unbiased which leads to large errors. Therefore, the adaptive sampling strategy for L^2 -distance loss is not suitable here.

In order to reduce the statistical errors from Monte Carlo approximation of the integrals, we can use importance sampling method. Specifically, for any time t_m , suppose that $S_m = \{x_m^j\}_{\{j=1, \dots, N\}}$ is sampled from distribution η_m , then the L_{kl} can be estimated by

$$\begin{aligned} L_{\text{kl}}(\rho_{NF, \theta}, \{\hat{\mu}_{t_m}\}_{\{m=0, \dots, M\}}) &= - \sum_{m=0}^M \int_{\mathbb{R}^d} \hat{\rho}_{t_m}(x) \log(\rho_{NF, \theta}(t_m, x)) dx \\ &= - \sum_{m=0}^M \int_{\mathbb{R}^d} \frac{\hat{\rho}_{t_m}(x) \log(\rho_{NF, \theta}(t_m, x))}{\eta_m(x)} \eta_m(x) dx \\ &\approx - \sum_{m=0}^M \frac{1}{N} \sum_{x \in S_m} \frac{\hat{\rho}_{t_m}(x) \log(\rho_{NF, \theta}(t_m, x))}{\eta_m(x)}. \end{aligned} \quad (21)$$

It can be found that if we choose η_m as η_m^* with the following density function:

$$\eta_m^*(x) = \frac{|\hat{\rho}_{t_m}(x) \log(\rho_{NF,\theta}(t_m, x))|}{\int_{\mathbb{R}^d} |\hat{\rho}_{t_m}(x) \log(\rho_{NF,\theta}(t_m, x))| dx},$$

the variance of the approximation is the smallest. However, we do not know the integral value in the denominator before we compute it. Therefore, our task is to find a computable and suitable $\eta_m(x)$ such that variance of the approximation decays. A reasonable choice here is $\eta_m(x) = \hat{\rho}_{t_m}(x)$. Although $\hat{\rho}_{t_m}(x)$ is probably not the best density to reduce the statistical error, we notice that in high-dimensional case, this density function can avoid the case that a large number of training points are located close to the boundary even if there are few simulated particles there. In this case, we need to use accept-reject to draw samples from $\hat{\rho}_{t_m}(x)$. In high-dimensional case, accept-reject sampling is expensive and with low efficiency. To avoid this, we can take $\eta_m(x) = \rho_{NF,\theta}(t_m, x)$. Since $\rho_{NF,\theta}(t_m, x)$ is a normalizing flow, we can directly draw samples from it.

For the loss function L_{path} (17), there is no statistical error when using this loss function, since we do not need to sample training sets to estimate it. Hence, we do not design an adaptive method for this loss function.

2.2.5 Summary of algorithms: classified by types of neural networks together with loss functions

The deepSPoC algorithms are summarized as follows. In Algorithm 1, we present the deepSPoC using fully connected neural network together with L^2 -distance loss function L_{sq} . We present both vanilla and adaptive deepSPoC in the Algorithm. By vanilla deepSPoC we mean the deepSPoC algorithm without using any special adaptive strategies introduced in Section 2.2.4.

In Algorithm 2, we present the deepSPoC using normalizing flow together with KL divergence loss function L_{kl} . We again show both vanilla and adaptive version in the algorithm. When $N_{\text{ada}} = 0$, Algorithm 2 presents a vanilla deepSPoC with normalizing flows. When $N_{\text{ada}} > 0$, in the 0th iteration, a Vanilla deepSPoC is implemented and in the rest iterations, an adaptive deepSPoC is implemented by applying importance sampling to the integrals in L function.

The deepSPoC algorithm with normalizing flow and loss function L_{path} is presented in the Algorithm 3.

Algorithm 1 Vanilla/adaptive deepSPoC algorithm with fully connected neural networks and loss function L_{sq}

Require: Initial distribution μ_0 , number of time intervals M , number of sampled particles K , number of uniform training points N_1 , number of adaptive training points N_2 , intensity of noise σ , pre-determined region Ω_0 , number of training epochs N_{epoch} , mollification scale ϵ , initial learning rate α_0 , contraction factor γ , step size Γ , and a fully connected neural network $\rho_{FC,\theta}$.

1: **for** $\text{epoch} = 1$ **to** N_{epoch} **do**
2: Decide the learning rate of this epoch $\alpha_{\text{epoch}} = \alpha_0 \gamma^{\lfloor \frac{\text{epoch}}{\Gamma} \rfloor}$.
3: Independently generate starting point set $\{X_{t_0}^i\}_{\{i=1, \dots, K\}}$ from μ_0 .
4: **for** $m = 1$ **to** M **do**
5: Simulate K paths of particles $\{X^i : i = 1, \dots, K\}$ by Euler scheme

$$X_{t_m}^i - X_{t_{m-1}}^i = b\left(t_{m-1}, X_{t_{m-1}}^i, \rho_{FC,\theta}(t_{m-1}, \cdot)\right) \Delta t + \sigma\left(t_{m-1}, X_{t_{m-1}}^i, \rho_{FC,\theta}(t_{m-1}, \cdot)\right) \Delta Z_t^i,$$
and store the paths.
6: **end for**
7: Sample the training points $S_{\text{uniform}} = \{x^j\}_{j=0}^{N_1}$ from a uniform distribution on Ω_0 .
8: **for** $m = 0$ **to** M **do**
9: **if** Vanilla **then**
10: Set training set as $S_m = S_{\text{uniform}}$.
11: **else**
12: **if** $\text{epoch} = 1$ **then**
13: Set training set as $S_m = S_{\text{uniform}}$.
14: **else**
15: Build set S_{adaptive}^m using path data $\{\hat{X}^j\}_{\{j=1, \dots, N_2\}}$ randomly selected from the last epoch's particle paths:

$$S_{\text{adaptive}}^m = \left\{ x_m^j \mid x_m^j = \hat{X}_{t_m}^j + \sigma \delta_j, j = 1, \dots, N_2 \right\}.$$

16: Set training set as S_m

$$S_m = S_{\text{uniform}}^m \cup S_{\text{adaptive}}^m,$$

17: **end if**
18: **end if**
19: **end for**
20: Calculate the loss function

$$\frac{1}{|S_m|} \sum_{m=0}^M \sum_{x \in S_m} \left| \rho_{FC,\theta}(t_m, x) - \frac{1}{K} \sum_{i=1}^K \frac{1}{(2\pi\epsilon^2)^{\frac{d}{2}}} e^{-\frac{|x - X_{t_m}^i|^2}{2\epsilon^2}} \right|^2$$

21: Calculate the gradient of the loss function with respect to θ and implement one step of gradient descent by Adam optimizer with learning rate α_{epoch} to update θ .
22: **end for**
23: Store and return the numerical solution.

Algorithm 2 Vanilla/adaptive deepSPoC algorithm with normalizing flows and loss function L_{kl}

Require: Initial distribution μ_0 , number of time intervals M , number of sampled particles K , number of training points N , pre-determined region Ω_0 , number of adaptive iteration N_{ada} , number of training epochs N_{epoch} , mollification scale ϵ , initial learning rate α_0 , contraction factor γ , step size Γ and a normalizing flow $\rho_{NF,\theta}$.

```

1: for ada to  $N_{\text{ada}}$  do
2:   for epoch = 1 to  $N_{\text{epoch}}$  do
3:     Decide the learning rate of this epoch  $\alpha_{\text{epoch}} = \alpha_0 \gamma^{\lfloor \frac{\text{epoch}}{\Gamma} \rfloor}$ .
4:     Independently generate starting point set  $\{X_{t_0}^i\}_{\{i=1, \dots, K\}}$  from  $\mu_0$ .
5:     for  $m = 1$  to  $M$  do
6:       Simulate  $K$  paths of particles  $\{X^i : i = 1, \dots, K\}$  by Euler scheme

$$X_{t_m}^i - X_{t_{m-1}}^i = b \left( t_{m-1}, X_{t_{m-1}}^i, \rho_{NF,\theta}(t_{m-1}, \cdot) \right) \Delta t + \sigma \left( t_{m-1}, X_{t_{m-1}}^i, \rho_{NF,\theta}(t_{m-1}, \cdot) \right) \Delta Z_t^i,$$

       and store the paths.
7:     end for
8:     for  $m = 0$  to  $M$  do
9:       if ada = 0 then
10:        Sample the training points  $S_m = \{x_m^j\}_{j=0}^N$  from a uniform distribution on  $\Omega_0$ .
11:       else
12:        Sample the training points  $S_m = \{x_m^j\}_{j=0}^N$  from the normalizing flow  $\rho_{NF,\theta}(t_m, \cdot)$ .
13:       end if
14:       At time  $t = t_m$ ,  $\forall x \in S_m$  compute the approximate density function by

$$\hat{\rho}_{t_m}(x) = \sum_{i=1}^K (2\pi)^{-\frac{d}{2}} \epsilon^{-d} \exp \left( -\frac{1}{2\epsilon^2} (x - X_{t_m}^i)^T (x - X_{t_m}^i) \right).$$

       and store  $\hat{\rho}_{t_m}$  value.
15:     end for
16:     if ada = 0 then
17:       Build the loss function

$$L_{\text{kl}} \left( \rho_{NF,\theta}, \{\hat{\mu}_{t_m}\}_{\{m=0, \dots, M\}} \right) = - \sum_{m=0}^M \frac{1}{N} \sum_{x \in S_m} \hat{\rho}_{t_m}(x) \log(\rho_{NF,\theta}(t_m, x)).$$

18:     else
19:       Build the loss function

$$L_{\text{kl}} \left( \rho_{NF,\theta}, \{\hat{\mu}_{t_m}\}_{\{m=0, \dots, M\}} \right) = - \sum_{m=0}^M \frac{1}{N} \sum_{x \in S_m} \frac{\hat{\rho}_{t_m}(x)}{\rho_{NF,\theta}(x)} \log(\rho_{NF,\theta}(t_m, x)).$$

20:     end if
21:     Calculate the gradient of the loss function with respect to  $\theta$  and implement one step of gradient descent by Adam optimizer with learning rate  $\alpha_{\text{epoch}}$  to update  $\theta$ .
22:   end for
23: end for
24: Store and return the numerical solution.

```

Algorithm 3 DeepSPoC algorithm with normalizing flows and loss function L_{path}

Require: Initial distribution μ_0 , number of time intervals M , number of sampled particles K , number of training epochs N_{epoch} , initial learning rate α_0 , contraction factor γ , step size Γ and a normalizing flow $\rho_{NF,\theta}$.

1: **for** epoch = 1 **to** N_{epoch} **do**

2: Decide the learning rate of this epoch $\alpha_{\text{epoch}} = \alpha_0 \gamma^{\lfloor \frac{\text{epoch}}{\Gamma} \rfloor}$.

3: Independently generate starting point set $\{X_{t_0}^i\}_{\{i=1, \dots, K\}}$ from μ_0 .

4: **for** $m = 0$ **to** M **do**

5: Simulate K paths of particles $\{X^i : i = 1, \dots, K\}$ by Euler scheme

$$X_{t_m}^i - X_{t_{m-1}}^i = b\left(t_{m-1}, X_{t_{m-1}}^i, \rho_{NF,\theta}(t_{m-1}, \cdot)\right) \Delta t + \sigma\left(t_{m-1}, X_{t_{m-1}}^i, \rho_{NF,\theta}(t_{m-1}, \cdot)\right) \Delta Z_t^i,$$

and store the paths.

6: **end for**

7: Build the loss function

$$-\sum_{m=0}^M \frac{1}{K} \sum_{i=1}^K \log(\rho_{NF,\theta}(t_m, X_{t_m}^i))$$

8: Calculate the gradient of the loss function with respect to θ and implement one step of gradient descent by Adam optimizer with learning rate α_{epoch} to update θ .

9: **end for**

10: Store and return the numerical solution.

3 Some theoretical analysis for deepSPoC

In the previous section, we have already introduced the motivation and the main idea of deepSPoC algorithm. Before showing the results of our numerical experiments, we provide some theoretical analysis for the algorithm. First, we give some convergence analysis of deepSPoC algorithm under some simplified conditions, especially when replacing the neural network with Fourier basis to approximate density function. It is well known that analyzing and proving the convergence of algorithms involving neural networks is very challenging, but we can prove the convergence of our algorithm when using Fourier basis instead of neural network to approximate the density function. We believe this convergence analysis will provide some theoretical basis for the effectiveness of the algorithm and explain how the learning rate, mollifier, loss function, and other factors affect the results of the algorithm. In the second subsection, we will have some discussion about the posterior error estimation of the deepSPoC algorithm, from which we can have an upper bound of how far our numerical solution is from the true solution. Most of the theoretical results in this section will only be stated, and their rigorous proofs will be shown in the appendix.

Here are some notations we use in this section. We denote by $\|\cdot\|$ the Frobenius norm of a matrix, by \mathcal{P}_p the space of all Borel probability measures μ on \mathbb{R}^d such that $\|\mu\|_p := (\int_{\mathbb{R}^d} |x|^p \mu(dx))^{1/p} < \infty$, and by $W_p(\mu, \nu)$ the p -Wasserstein distance for $\mu, \nu \in \mathcal{P}_p$ defined as

$$W_p(\mu, \nu) = \inf\{(\mathbb{E}|X - Y|^p)^{1/p} : X \sim \mu, Y \sim \nu\}.$$

3.1 Convergence analysis of deepSPoC when approximating density functions with Fourier basis (revising)

Whether using fully connected neural networks or Fourier basis to approximate density functions, it is easy to see that the results of the approximation are not strictly probability density functions (it has negative parts and its integral is not equal to 1 in general). Therefore, to rigorously analyze the convergence, we introduce the “rectification” of these functions to make them become real probability density functions.

Definition 3.1. For a pre-determined truncated region $\Omega_0 \in \mathbb{R}^d$, if a continuous function $\rho : \Omega_0 \rightarrow \mathbb{R}$ (or continuous function $\rho : \mathbb{R}^d \rightarrow \mathbb{R}$) satisfies that $0 < \int_{\Omega_0} (\rho(x) \vee 0) dx < \infty$, then we define its “rectification” to be a probability density function $R(\rho)(x)$ on \mathbb{R}^n in the following way

$$R(\rho)(x) = \begin{cases} \frac{\rho(x) \vee 0}{\int_{\Omega_0} \rho(x) \vee 0 dx} & \text{if } x \in \Omega_0, \\ 0 & \text{if } x \notin \Omega_0. \end{cases}$$

It is easy to verify that if ρ can be rectified, then $R(\rho)$ is a probability density function.

In the rest of this subsection (also in the proofs of results in this subsection which are shown in appendix), unless ρ is already a true probability density function, $b(t, X, \rho)$ (resp. $\sigma(t, X, \rho)$) should always be regarded as $b(t, X, R(\rho))$ (resp. $\sigma(t, X, R(\rho))$) when the truncated region Ω_0 is specified and ρ can be rectified. In addition, the p -Wasserstein distance $W_p(\rho_1, \rho_2)$ and $\|\rho_1\|_p$ should also be regarded as $W_p(R(\rho_1), R(\rho_2))$ and $\|R(\rho_1)\|_p$ respectively, if ρ_1 and ρ_2 need to be rectified to be a true probability density function. We point out that this kind of “rectification” is natural because the rectified distribution $R(\rho)$ is equivalent to the distribution obtained by applying accept-reject sampling to the original function ρ (as long as we “refuse” all the negative parts), and it is actually what we did in our numerical experiments if we need to sample from a function which is not a probability density function.

The interacting particle system we consider in this subsection use Fourier basis as approximation framework and we assume the SDEs are driven by Brownian motions. The system takes the following form:

$$\begin{cases} dX_t^{i,n} = b\left(t, X_t^{i,n}, \rho_{\theta_t^{n-1}}(\cdot)\right) dt + \sigma\left(t, X_t^{i,n}, \rho_{\theta_t^{n-1}}(\cdot)\right) dB_t^{i,n}, i = 1, \dots, K \\ \rho_{\theta_t^n} = F\left(\rho_{\theta_t^{n-1}}, \hat{\mu}^n, \alpha_n\right), \end{cases} \quad (22)$$

where $X_0^{i,n}$ ($i = 1, \dots, K; n \geq 1$) are i.i.d. \mathbb{R}^d random variables with the given initial distribution μ_0 , and the operator F determines how to update parameters which is similar to the operator F in (9) whose definition will be specified later. The pre-determined truncated region is set as $\Omega_0 = [-L, L]^d$, then for $t \in [0, T]$, the function $\rho_{\theta_t^n}$ which can be rectified is a linear combination of finite Fourier basis functions $\{e_\nu\}_{\{\nu=1, \dots, N\}}$ on Ω_0 , i.e., $\rho_{\theta_t^n} = \sum_{\nu=1}^N \theta_t^\nu e_\nu$. Here we do not consider the error introduced by discretization of time for simplicity, so it might seem a bit strange that the parameters θ is continuously depend on time t . However, once time is discretized, the number of parameters also becomes finite, which is equivalent to approximating the density function using Fourier bases at each discrete time point.

For any given $0 < \epsilon < 1$ as a precision requirement, we define a new mollifier \tilde{f}_ϵ in the following way

$$\tilde{f}_\epsilon(x) = \frac{\tilde{C}}{\epsilon^d} \left(1 - \frac{|x|}{\epsilon}\right) \cdot 1_{\{|x| \leq \epsilon\}},$$

where $\tilde{C} = \tilde{C}(d)$ is a constant to make sure that the integral of \tilde{f}_ϵ is 1. We use this mollifier instead of the Gaussian mollifier f_ϵ in this subsection. Since \tilde{f}_ϵ has compact support, using this mollifier on the truncated region Ω_0 can bring some convenience to our analysis without causing any essential difference.

We denote $\tilde{X} := X \cdot 1_{\{X \in [-(L-\epsilon), L-\epsilon]^d\}}$ for the truncated particle, and $\delta_{\tilde{X}}^\epsilon := \delta_X * \tilde{f}_\epsilon$ for the mollified particle. Although in most cases the initialization of $\rho_{\theta_0^t}$ will not effect the final result of the algorithm, but for simplicity, here we choose $\rho_{\theta_0^t} = P_N\left(\left(\frac{1}{K} \sum_{i=1}^K \delta_{\tilde{X}_t^{i,0}}\right) * \tilde{f}_\epsilon\right) = P_N\left(\frac{1}{K} \sum_{i=1}^K \delta_{\tilde{X}_t^{i,0}}^\epsilon\right)$, where $X_t^{i,0} = X_0^{i,0} \sim \mu_0$, P_N denotes the orthogonal projection mapping that project the density function (viewed as an element in $L^2(\Omega_0)$) to the subspace expanded by N Fourier basis functions.

The method of updating the parameters (which we denoted by operator \tilde{F}) is defined similar to the neural network case, which can be divided into the following three steps. First, we mollify the empirical measure formed by a batch of truncated particles at each time t , i.e.

$$\hat{\rho}_t = \left(\frac{1}{K} \sum_{i=1}^K \delta_{\tilde{X}_t^{i,n}}\right) * \tilde{f}_\epsilon,$$

we use the truncated particles to make sure the support of $\hat{\rho}_t$ is in Ω_0 . We will prove that if Ω_0 is sufficiently large, then we can neglect particles that occasionally appear outside the region. Second, we calculate $\|\rho_{\theta_{n-1}^t} - \hat{\rho}_t\|_{L_2}^2$ as loss function. Third, we calculate the gradient of θ_{n-1}^t with respect to this loss, and apply one step of gradient descent with learning rate α_n . But since we use the linear basis instead of neural network to approximate the density function in this case, we can express the \tilde{F} explicitly. Indeed, if we assume that $P_N(\hat{\rho}_t) = \sum_{\nu=1}^N \hat{\theta}_\nu e_\nu$, then we will find

$$\nabla_{\theta_{n-1}^t} \|\rho_{\theta_{n-1}^t} - \hat{\rho}_t\|_{L_2}^2 = \nabla_{\theta_{n-1}^t} \|\rho_{\theta_{n-1}^t} - P_N(\hat{\rho}_t)\|_{L_2}^2 = \nabla_{\theta_{n-1}^t} \sum_{\nu=1}^N |\theta_\nu^t - \hat{\theta}_\nu|^2 = 2(\theta_{n-1}^t - \hat{\theta}).$$

With learning rate α_n , it's easy to verify that \tilde{F} have the following expression

$$\begin{aligned}\rho_{\theta_n^t} &= \tilde{F}\left(\rho_{\theta_{n-1}^t}, \frac{1}{K} \sum_{i=1}^K \delta_{X_t^{i,n}}, \alpha_n\right) \\ &= \sum_{\nu=1}^N (\theta_\nu^t - 2\alpha_n(\theta_\nu^t - \hat{\theta}_\nu)) e_\nu \\ &= (1 - 2\alpha_n)\rho_{\theta_{n-1}^t} + 2\alpha_n P_N(\hat{\rho}_t),\end{aligned}\tag{23}$$

therefore we can compute recursively to obtain that

$$\rho_{\theta_{n-1}^t} = \sum_{l=0}^{n-1} \beta_l P_N\left(\frac{1}{K} \sum_{i=1}^K \delta_{X_t^{i,l}}^\epsilon\right) = P_N\left(\sum_{l=0}^{n-1} \frac{\beta_l}{K} \sum_{i=1}^K \delta_{X_t^{i,l}}^\epsilon\right),\tag{24}$$

where $\beta_l = (1 - 2\alpha_{n-1})(1 - 2\alpha_{n-2}) \dots (1 - 2\alpha_{l+1})2\alpha_l$ is the weight of l -th batch of particles and satisfy that $\sum_{l=0}^{n-1} \beta_l = 1$.

If we choose the number of basis functions N large enough, then $P_N(\hat{\rho}_t) \approx \frac{1}{K} \sum_{i=1}^K \delta_{X_t^{i,n}}$, therefore F can be approximately viewed as a weighted average, which brings us back to the original SPoC case (8). In fact, it's easy to see that $\hat{\rho}_t$ is Lipschitz continuous function with a uniform Lipschitz constant $\frac{\tilde{C}}{K\epsilon^{d+1}}$, then its truncation of the Fourier series will provide uniform approximation (cf. [28]):

$$\|\hat{\rho}_t - P_N(\hat{\rho}_t)\|_\infty \leq C(\epsilon, K, L, d) \frac{(\log N)^d}{N}.$$

Then in the following discussion, $N = N(\epsilon, K, L, d)$ will always be chosen to satisfy that for all Lipschitz continuous density function ρ with its Lipschitz constant less than $\frac{\tilde{C}}{K\epsilon^{d+1}}$,

$$\|\rho - P_N(\rho)\|_\infty \leq \frac{\epsilon}{(2L)^{d+1}},\tag{25}$$

when N satisfies the assumption above, then it follows easily from the definition of the W_1 distance and $\|\cdot\|_1$ that

$$W_1(\rho, P_N(\rho)) \leq \epsilon; \|\rho\|_1 - \|P_N(\rho)\|_1 \leq \epsilon.\tag{26}$$

Here is a remark about why we choose W_1 distance here to measure the convergence, that is because the W_1 distance between two distribution can be controlled by the supreme norm distance (or L^2 distance) between their density function in a more "direct" way. Otherwise, we can still obtain such control like the following form (cf. Lemma 3.2 in [15])

$$W_r^r(\rho, P_N(\rho)) \leq C_{r,L} \|\rho - P_N(\rho)\|_\infty,$$

we can see such control is not homogeneous when $r \neq 1$, therefore, for the simplicity of our results and discussion, we choose W_1 distance to measure the distance between two distributions in this subsection.

With the above preparations, the system (22) is now close to the system in the original SPoC paper [15], so its convergence can also be proved with a similar method. To rigorously prove the convergence and quantify the error to the real solution, we also need the following assumption:

Assumption 3.1. *There exists a constant $C \geq 0$ such that*

$$\begin{aligned}|b(t, x, \mu) - b(t, y, \nu)| + \|\sigma(t, x, \mu) - \sigma(t, y, \nu)\| &\leq C(|x - y| + W_1(\mu, \nu)), \\ |b(t, 0, \mu)| + \|\sigma(t, 0, \mu)\| &\leq C(1 + \|\mu\|_1)\end{aligned}$$

for all $t \in [0, T]$, $x, y \in \mathbb{R}^d$, $\mu, \nu \in \mathcal{P}_1$.

The above assumption ensures the well-posedness of strong solution of the system (22) and its mean-field limit equation (cf. [3, 29]). Furthermore, assumption 3.1 also provides some prior estimates of the particles of system (22) (see proposition 3.2), from which we will find that the distributions of SPoC particles are uniformly compact in a certain sense, therefore we can choose a bounded region Ω_0 to truncate them during the training process.

Proposition 3.2. *Let assumption 3.1 be satisfied, $\mu_0 \in \mathcal{P}_3$, and assume N is chosen to satisfy (25), then there exists a constant C_0 independent of L such that for any $X_t^{i,n}$ in system (22),*

$$\mathbb{E} \left(\sup_{0 \leq s \leq T} |X_s^{i,n}|^3 \right) \leq C_0,$$

and

$$\mathbb{E} \left(\mathbf{1}_{\{\sup_{0 \leq s \leq T} |X_s^{i,n}|^2 \geq L_0\}} \cdot \sup_{0 \leq s \leq T} |X_s^{i,n}|^2 \right) \leq \frac{C_0}{L_0}.$$

By proposition 3.2, we can find that it is reasonable to have a uniform truncation of space for all SPoC particles. Now we begin to state our final result of convergence. We assume for simplicity that now α_n is chosen to make all β_l the same, i.e., equal $\frac{1}{n}$, which is the case that all the particles have the equal weights. For more general cases of weights which will also have convergence result, we refer readers to the original SPoC paper [15]. The following is our main convergence theorem.

Theorem 3.3. *Under assumption 3.1 and assume $\mu_0 \in \mathcal{P}_3$, N is chosen to satisfy (25), the weight of the l -th batch of particles $\beta_l = \frac{1}{n}$ ($l = 0, \dots, n-1$), and L , which decides the truncated region Ω_0 , is chosen to satisfies that for any $n = 0, 1, 2, \dots$,*

$$\mathbb{E} \left(\sup_{0 \leq s \leq T} |X_s^{i,n} - \tilde{X}_s^{i,n}|^2 \right) \leq \epsilon^2, \quad (27)$$

then there exists a constant C independent of n, K, L, ϵ such that

$$\mathbb{E} W_1^2(\rho_{\theta_{n-1}^t}, \mu_t) \leq C(\epsilon^2 + (Kn)^{-\frac{1}{1+d/2}}).$$

3.2 Posterior error estimation

A posterior error estimation of the algorithm is important from both theoretical and practical perspectives, it can tell us how close our numerical solution is to the exact solution during the training process, so we can use it to verify our solution or to decide when to stop training. Its usual form is to provide an upper bound on the distance between the current solution we compute and the true solution. For example, the Physics-informed neural networks (PINNs) usually use the training error (i.e. the residual obtained by substituting the neural network-fitted solution into the model's equation) to get an estimation of the generalization error, see for instance [30, 31, 32]. For deepSPoC algorithm, however, we have said that the loss of deepSPoC during the training process can not be used to estimate the error, so we need to explore other quantities to give a posterior error estimation. Similar to the case of PINNs, we can substituting the neural network-fitted density function into the mean-field SDE and solve it (note that at this point the SDE becomes Markovian and therefore can be easily simulated), and by comparing the distance between the density of this solution and the neural network-fitted density we put into, we can give our posterior error estimation.

To rigorously state and prove the result, we need some assumptions about the mean-field SDE. First, we still restrict the type of the diffusion term of the SDE that it is driven by Brownian motion, which reads the following form:

$$dX_t = b(t, X_t, \text{Law}(X_t))dt + \sigma(t, X_t, \text{Law}(X_t))dB_t, \quad (28)$$

where $\text{Law}(X_t)$ denotes the distribution of X_t , and the initial distribution is given as $X_0 \sim \bar{\mu} \in \mathcal{P}_2$. Furthermore, the b and σ in the above equation should satisfy the following assumption:

Assumption 3.2. *There exists a constant $C \geq 0$ such that*

$$\begin{aligned} |b(t, x, \mu) - b(t, y, \nu)| + \|\sigma(t, x, \mu) - \sigma(t, y, \nu)\| &\leq C(|x - y| + W_2(\mu, \nu)), \\ |b(t, 0, \mu)| + \|\sigma(t, 0, \mu)\| &\leq C(1 + \|\mu\|_2) \end{aligned}$$

for all $t \in [0, T]$, $x, y \in \mathbb{R}^d$, $\mu, \nu \in \mathcal{P}_2$.

Remark 5. *From the basic property of Wasserstein distance we know that $W_1(\mu, \nu) \leq W_2(\mu, \nu)$ and $\|\mu\|_1 \leq \|\mu\|_2$, therefore Assumption 3.2 is actually weaker than Assumption 3.1 in the last subsection.*

In this subsection, we view the time-dependent density function as a map from $[0, T]$ to \mathcal{P}_2 and denote it by μ_\cdot . We denote by $\mathcal{P}_{2,\infty}([0, T])$ the space consists of all such \mathcal{P}_2 valued maps $\mu_\cdot : [0, T] \rightarrow \mathcal{P}_2$ which is continuous for the W_2 -distance. Specifically, $\mu_\cdot \in \mathcal{P}_{2,\infty}([0, T])$ satisfies that $\sup_{0 \leq t \leq T} \|\mu_t\|_2 < \infty$. Our numerical solution $\rho_{FC, \theta}(t, x)$ can also be considered in this space. We further introduce the following metric to make $\mathcal{P}_{2,\infty}([0, T])$ a metric space:

Definition 3.4. *For $\mu_\cdot, \nu_\cdot \in \mathcal{P}_{2,\infty}([0, T])$, $\alpha > 0$, define*

$$H_\alpha(\mu_\cdot, \nu_\cdot) := \left(\int_0^T e^{-\alpha t} W_2^2(\mu_t, \nu_t) dt \right)^{\frac{1}{2}}.$$

It is easy to verify that H_α is a metric on $\mathcal{P}_{2,\infty}([0, T])$ and specifically, it satisfies triangle inequality.

When given $\mu_* \in \mathcal{P}_{2,\infty}([0, T])$, the Markovian SDE

$$dX_t = b(t, X_t, \mu_t)dt + \sigma(t, X_t, \mu_t)dB_t, X_0 \sim \bar{\mu}$$

will have a strong solution $(X_t)_{0 \leq t \leq T}$ such that the map $t \in [0, T] \mapsto \text{Law}(X_t)$ which is denoted by $\Phi(\mu_*)$ is in the space $\mathcal{P}_{2,\infty}([0, T])$ under Assumption 3.2. We see that we have defined a map $\Phi : \mathcal{P}_{2,\infty}([0, T]) \rightarrow \mathcal{P}_{2,\infty}([0, T])$, the next proposition will show that when α is set properly, Φ can be a contraction map of the metric space $\mathcal{P}_{2,\infty}([0, T])$ combines with metric H_α .

Proposition 3.5. *Let Assumption 3.2 is satisfied and the initial distribution $\bar{\mu} \in \mathcal{P}_2$, let $C_0 = 2(T + 1)C^2$, where C is the constant in the Assumption 3.2, and assume $\alpha > C_0$, then for any $\mu_*, \nu_* \in \mathcal{P}_{2,\infty}([0, T])$, we have*

$$H_\alpha(\Phi(\mu_*), \Phi(\nu_*)) \leq \sqrt{\frac{C_0}{\alpha - C_0}} H_\alpha(\mu_*, \nu_*).$$

The proof of this proposition will be given in the appendix.

Furthermore, under Assumption 3.2, the solution of (28) can also be related to an element in $\mathcal{P}_{2,\infty}([0, T])$, we denote it by μ^* . It is easy to see that μ^* is a fixed point of Φ . Utilize the contraction of Φ when $\alpha > 2C_0$, we can have the following posterior error estimation:

Theorem 3.6. *Let Assumption 3.2 is satisfied and the initial distribution $\bar{\mu} \in \mathcal{P}_2$, let μ^* is the distribution function over $[0, T]$ of the solution of (28), and let $\alpha > 2C_0 = 4(T + 1)C^2$, then for any $\mu_* \in \mathcal{P}_{2,\infty}([0, T])$, we have the following estimate*

$$H_\alpha(\mu_*, \mu^*) \leq \left(1 - \sqrt{\frac{C_0}{\alpha - C_0}}\right)^{-1} H_\alpha(\mu_*, \Phi(\mu_*)).$$

Proof. By Proposition 3.5 and triangle inequality of metric H_α , we have

$$\begin{aligned} H_\alpha(\mu_*, \mu^*) &\leq H_\alpha(\mu_*, \Phi(\mu_*)) + H_\alpha(\Phi(\mu_*), \mu^*) \\ &= H_\alpha(\mu_*, \Phi(\mu_*)) + H_\alpha(\Phi(\mu_*), \Phi(\mu^*)) \\ &\leq H_\alpha(\mu_*, \Phi(\mu_*)) + \sqrt{\frac{C_0}{\alpha - C_0}} H_\alpha(\mu_*, \mu^*), \end{aligned}$$

then the conclusion follows from this. \square

4 Numerical experiments

In this section, we apply deepSPoC algorithm to different types of equations to test our algorithm. The numerical experiments we choose for testing cover mean-field SDEs with different spatial dimensions and different forms of b and σ , and the corresponding degenerate or non-local nonlinear PDEs. Notice that these characteristics often lead to difficulties when we consider solving them numerically, therefore we believe good performance of deepSPoC over these problems strongly demonstrates its effectiveness, extensiveness and strength.

Unless otherwise specified, in all the following experiments the fully connected neural network $\rho_{FC,\theta}$ we use is always with 6 hidden layers and each hidden layers consists of 512 neurons. Recall that this neural network is to fit the density function changes over time, and we have introduced its structure and activation function (without specification, we choose ReLU as the activation function) in section 2.2. For the temporal KRnet, we use 10 affine coupling blocks. Each affine coupling block has two fully connected hidden layers with each hidden layer consists of 512 neurons. We also use ReLU as the activation function in each hidden layers in tempreal KRnet. Here is a remark about the depth and the number of neurons we choose, that is we do not want our neural network to have too few parameters, such as using 32 neurons per layer instead of 512 neurons, though in many experiments we find that deepSPoC with such smaller network can also perform well. It is because in deepSPoC the function of neural network is to store the position of particles, so if the number of parameters in the network is too small, it seems hard to convince that the network can retain all the necessary information carried by the numerous particles we simulate.

We apply Adam method as our optimizer for updating the network's parameters, and all the numerical experiments are implemented with Pytorch.

4.1 Porous medium equations

Our first numerical experiment is to compute the following porous medium equation (PME)

$$\partial_t \rho = \Delta \rho^m.$$

It is a quasilinear degenerate parabolic equation, which degenerates when $\rho = 0$. The classical smooth solution may not exist for this equation in general, therefore we consider the weak energy solution instead. A famous weak solution to PME is Barenblatt solution (29), from which we can find that this weak solution loses classical derivative when the solution met the interface of $\rho = 0$. For $m > 1$, the Barenblatt solution is defined by

$$U_{m,C}(t, x) = \frac{1}{t^\alpha} \left\{ \left(C - \frac{m-1}{2m} \cdot \frac{\beta|x|^2}{t^{2\beta}} \right)^+ \right\}^{\frac{1}{m-1}} \quad (29)$$

where $x \in \mathbb{R}^d$, $\alpha = \frac{d}{d(m-1)+2}$, $\beta = \frac{\alpha}{d}$, and we set $m = 3$, $C = \frac{\sqrt{3}}{15}$ for our experiments. We choose an initial time $t_0 > 0$, and use the $U_{m,C}(t_0, \cdot)$ as the initial condition of PME, then apply deepSPoC to solve the PME with this initial condition during time interval $[t_0, t_0 + T]$. We compare our numerical solution at the terminal time $t_0 + T$ with the true solution $U_{m,C}(t_0 + T, \cdot)$, and show the comparison results by intuitive image of the solutions and quantitative error curve changes with epochs.

It can be noticed that the integration of Barenblatt solution (29) with respect to x which is independent of t does not equals 1, therefore we need to normalize it in order to make it a probability density. We denote the normalization constant by $c_0 = c_0(m, C, d) = \int_{\mathbb{R}^d} U_{m,C}(t, x) dx$. It can be easily verified that the normalized Barenblatt solution $\frac{1}{c_0} U_{m,C}(t, x)$ satisfies the following PDE

$$\partial_t \rho = \nu \Delta \rho^m, \quad (30)$$

where $\nu = c_0^{m-1}$. To apply deepSPoC algorithm to this equation, in the following experiments we always associate the above PDE (30) with the following density dependent SDE (except for section 4.1.5 where we associate (30) with an ODE)

$$dX_t = \sqrt{2\nu} \rho^{\frac{m-1}{2}}(t, X_t) dB_t \quad (31)$$

with given (normalized) initial distribution $\rho_{NN, \theta}(0, \cdot) = \frac{1}{c_0} U_{m,C}(t_0, \cdot)$. Then We use deepSPoC to compute (31) during a time span of length T . We use relative L^2 error to quantify the distance between the numerical solution and the real solution at the terminal time and estimate it by Monte Carlo integration, i.e.,

$$\frac{\|c_0 \rho_{NN, \theta}(T, \cdot) - U_{m,C}(t_0 + T, \cdot)\|_2}{\|U_{m,C}(t_0 + T, \cdot)\|_2} \approx \frac{\sqrt{\sum_{i=1}^{N_e} (c_0 \rho_{NN, \theta}(T, x_i) - U_{m,C}(t_0 + T, x_i))^2}}{\sqrt{\sum_{i=1}^{N_e} U_{m,C}(t_0 + T, x_i)^2}}, \quad (32)$$

where $\{x_i\}$, $i = 1, \dots, N_e$ are uniformly sampled from a predetermined region Ω_0 , and we set $N_e = 10^5$.

We first apply deepSPoC to compute PMEs with different dimensions according to the SDE (31), then we also try the deterministic particle method together with deepSPoC to solve PMEs. Detailed experimental parameters and the corresponding results for every experiment is shown respectively below.

4.1.1 1D PME

In this case we solve PME with one-dimensional spatial variables by deepSPoC with fully connected neural network(Algorithm 1 uniform version). We choose initial time $t_0 = 1$ and the total time span $T = 1$. The time discretization scale is chosen as $\Delta t = 0.01$. The number of training points N for each epoch is 1000 and it is sampled uniformly in a truncated region $\Omega_0 = [-2, 2]$. The number of sampled particles (or batch size) K is 1000. It can be referred back to section 2.2 for the specific meanings of K and N . For optimizer's setting, the initial learning rate is 0.001 and it is reduced to half every 500 epochs. The parameter ϵ for the Gaussian mollifier in (5) is 0.01.

Fig. 3(a) shows the image of numerical solution and real solution at the terminal time after 7000 epochs. The green line is the given initial condition $U_{m,C}(t_0, \cdot)$, the orange line is the numerical solution $c_0 \rho_{FC, \theta}(T, \cdot)$ (multiplied by the normalization constant c_0), and the blue line is the Barenblatt solution at terminal time $U_{m,C}(t_0 + T, \cdot)$ which is our target. We can see that our numerical solution is already very close to the true solution, except for some parts in the middle that do not completely overlap. The relative L^2 error of terminal time (see (32) for definition) changes with epochs is shown in Fig. 3(b), from which we can see the error shows a fluctuating downward trend with epochs and becomes stable after about 5000 epochs.

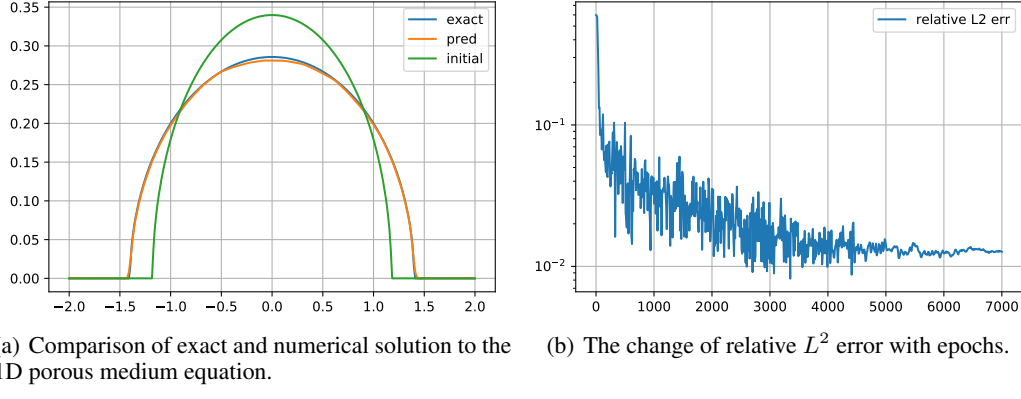


Figure 3: Result of 1D porous medium equation computed by deepSPoC with fully connected neural networks and loss function L_{sq} .

4.1.2 3D PME

When solving PME with three-dimensional spatial variables by deepSPoC with fully connected neural network(Algorithm 1 adaptive version), we set initial time $t_0 = 0.1$, time span $T = 0.2$, time discretization size $\Delta t = 0.005$. Notice that the Barenblatt solution changes dramatically as t approaches 0, so here we need to shorten the time span and decrease the time discretization size accordingly.

One major difference of 3D case compared with 1D case is now we need self-adaptive strategy to choose training set. Recall the notation in section 2.2.4, here we set $N_1 = 2000$, $N_2 = 2000$, and the intensity of the noise σ added to the adaptive training set is set to 0.2, and the region Ω_0 from which we sample training points is $[-2, 2]^3$. Other settings includes the sample number $K = 4000$ and the initial learning rate 0.001 which will be reduced to half every 500 epochs. The parameter ϵ for the Gaussian mollifier is set to 0.02. Typically, as the dimensionality increases, ϵ needs to be appropriately increased; otherwise, the height of the peaks obtained after mollifying each particle will become too high, making it difficult for the neural network to learn from the particles.

Fig. 4(a) shows the cut view with respect to the first spatial variable of numerical solution and real solution after 8000 epochs. Specifically, the green line is the cut of the initial condition, which is $U_{m,C}(0.1, \cdot, 0, 0)$, where the second and the third spacial variables are fixed to 0. Similarly, the blue line is the image of function $U_{m,C}(0.3, \cdot, 0, 0)$ and the orange line is the cut of our numerical solution which is $c_0 \rho_{FC,\theta}(0.2, \cdot, 0, 0)$. The relative L^2 error with epochs is shown in Fig. 4(b).

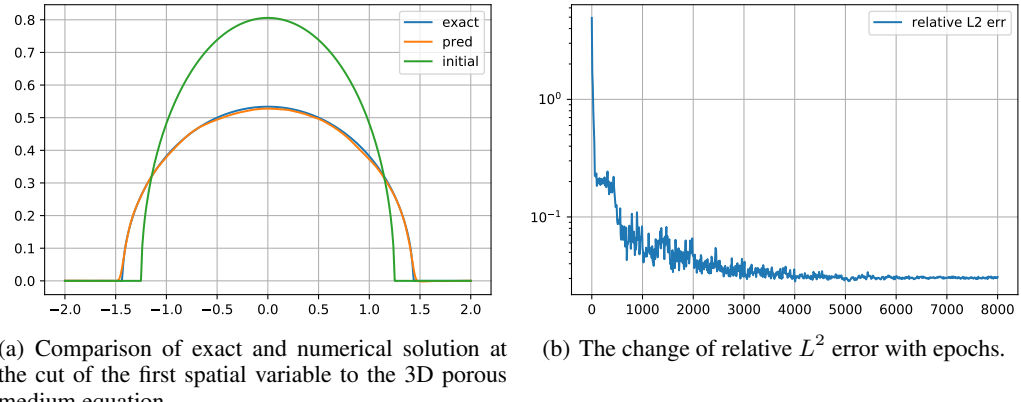


Figure 4: Result of 3D porous medium equation by deepSPoC with fully connected neural network and loss function L_{sq} .

4.1.3 5D PME

For the experiment of solving PME with five-dimensional spatial variables, we consider both deepSPoC with fully connected neural network(Algorithm 1 adaptive version) and deepSPoC with path data(Algorithm 3). For both algorithms, we set initial time $t_0 = 1$, time span $T = 1$ and time discrete size $\Delta t = 0.02$. In Algorithm 1, the total number of training points is 6000 consists of 2000 uniform training points and 4000 self-adaptive training points, and the noise added to the self-adaptive training points has intensity $\sigma = 0.3$. ϵ for the mollifier is set to 0.05. For both algorithms, the sample number K is 8000 and the predetermined region is $\Omega_0 = [-3, 3]^5$. The initial learning rate of optimizer is still 0.001, but now it is multiplied by a bigger contraction coefficient $\gamma = 0.7$ (which is 0.5 for 1D and 3D case) for every $\Gamma = 500$ epochs (recall section 2.2.3 for the roles γ and Γ play).

The computing result of Algorithm 1 after 12000 epochs and the relative L^2 error changes with epochs is shown in Fig. 5(a) and Fig. 5(b) respectively. Fig. 5(a) is still the cut of the first spacial variable, we can see that the numerical solution (orange line) and the real solution (blue line) almost coincide, both at the non-smooth interface and the smooth region in the middle.

The computing result of Algorithm 3 after 5000 epochs and the relative L^2 error changes with epochs is shown in Fig. 6(a) and Fig. 6(b) respectively. Comparing the numerical results and L_2 errors, we find that for this 5D PME, both Algorithm 3 and Algorithm 1 can solve this problem and the numerical solution of Algorithm 1 is more accurate than that of Algorithm 3.

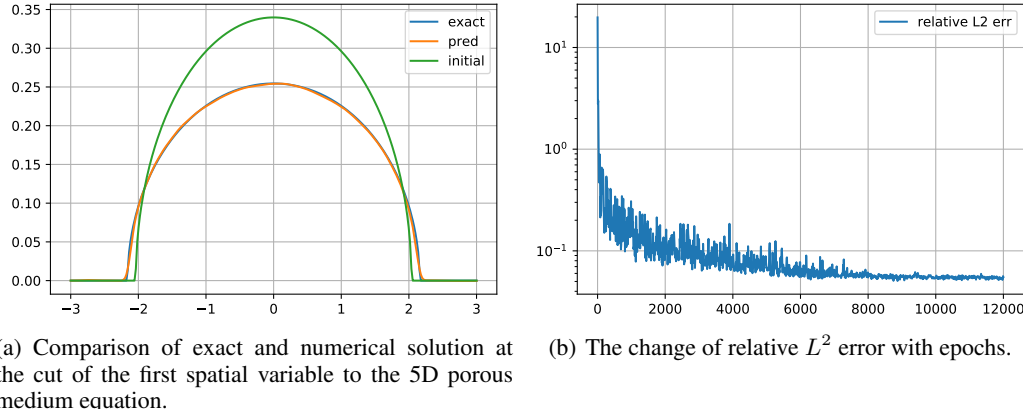


Figure 5: Result of 5D porous medium equation computed by deepSPoC with fully connected neural networks.

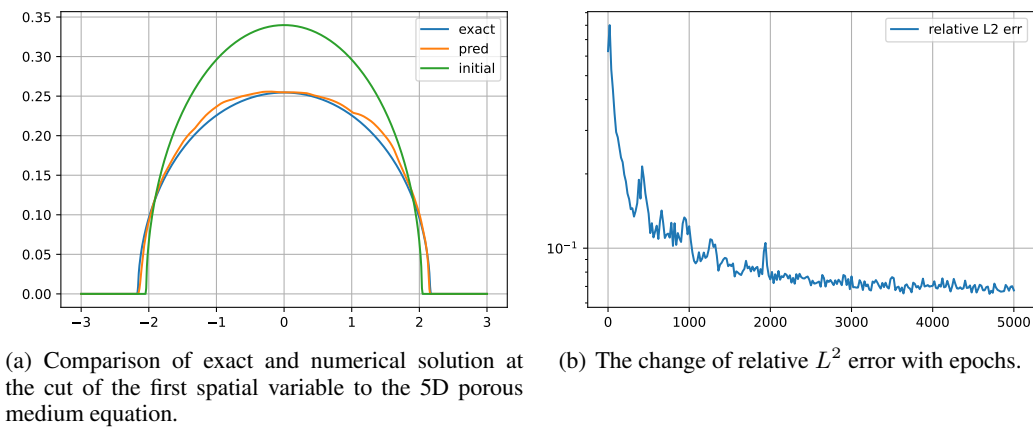


Figure 6: Result of 5D porous medium equation computed by deepSPoC with normalizing flows and loss function L_{path} defined by (17).

4.1.4 6D and 8D PME

For the experiment of solving PME with six and eight-dimensional spatial variables, we present the numerical result of deepSPoC with path data(Algorithm 3). We find it is hard to use Algorithm 3 to address high-dimensional problem such as 6D and 8D PME. The reason is that high-dimensional mollification can be inaccurate. Since there is no mollification in Algorithm 3, it is more suitable to be used to solve high-dimensional problem. For both 6D PME and 8D PME, we set initial time $t_0 = 1$, time span $T = 1.5$ and time discrete size $\delta t = 0.025$. The total number of samples is 10000. and the predetermined region is $\Omega_0 = [-3, 3]^6$ and $\Omega_0 = [-3, 3]^8$ respectively. The initial learning rate of optimizer is 0.001 and contraction coefficient $\gamma = 0.5$ for every $\Gamma = 500$ epochs.

We again run 5000 epochs for both 6D and 8D PME. The numerical solutions and the relative L^2 errors are presented in Fig 7(a), Fig 7(b), Fig 8(a) and Fig 8(b) respectively. The numerical results suggest Algorithm 3 can address high-dimensional problems with reasonable accuracy.

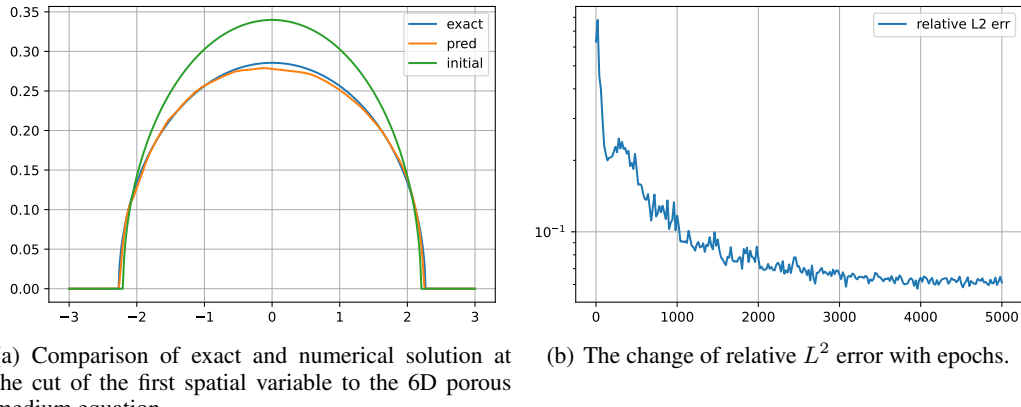


Figure 7: Result of 6D porous medium equation computed by deepSPoC with normalizing flows and loss function L_{path} .

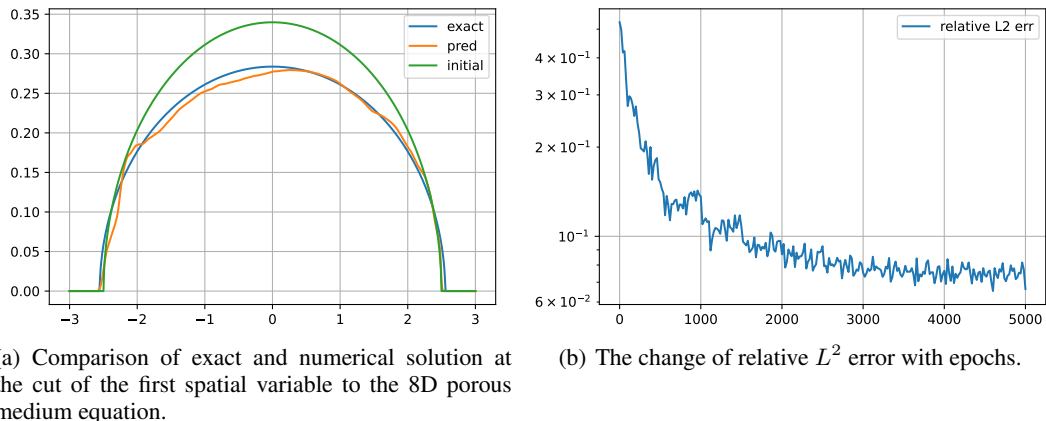


Figure 8: Result of 8D porous medium equation computed by deepSPoC with normalizing flows and loss function L_{path} .

4.1.5 DeepSPoC based on deterministic particle method for porous medium equations

As we have mentioned, we can also associate the PDE (30) with an ODE and apply deepSPoC to solve it. The ODE has the following form:

$$dX_t = \nu m \rho^{m-2}(X_t) \nabla \rho(X_t) dt. \quad (33)$$

Like stochastic particle methods that include SDEs, method using the ODE (33) is usually referred to as the deterministic particle method. Here we use the same ODE as in [4], in that paper this deterministic particle method is also interpreted as the gradient flow of distribution with respect to the Wasserstein distance. Our experimental results show that our method is flexible enough that can be based on not only stochastic particle methods, but also deterministic particle methods.

It can be noticed that the equation (33) involves taking the derivative of the density function, therefore we need to use a smooth neural network to fit the density function. We use SoftPlus function as our activation function in this experiment instead of ReLU function. The SoftPlus function can be viewed as a smooth approximation to the ReLU function, which is defined by

$$\text{SoftPlus}(x) = \frac{1}{\beta} \log(1 + \exp(\beta x)),$$

where the parameter β is set to 20 in our experiments. We obtain the derivatives by using PyTorch's automatic differentiation. We apply deepSPoC with fully connected neural network(Algorithm 1 uniform and adaptive version) to 1D and 3D PME. The other training parameters are exactly the same as in the previous experiments of 1D and 3D PME. The results is shown in Fig. 4.1.5, we can see that deepSPoC based on the deterministic particle method is still effective.

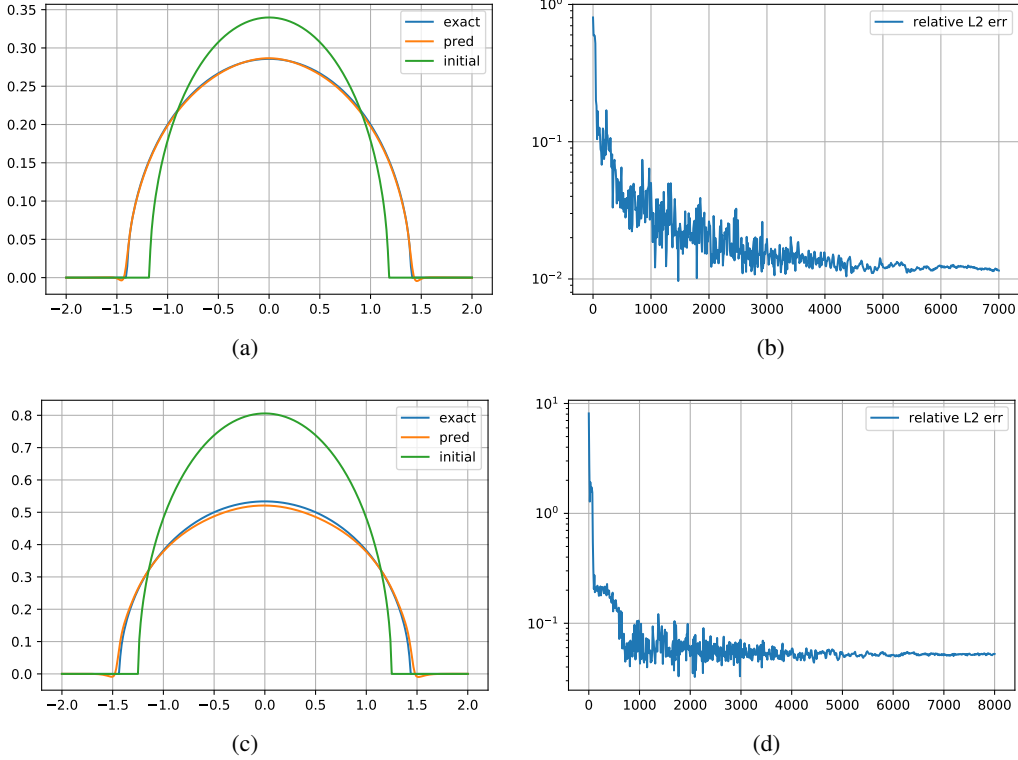


Figure 9: Results of deepSPoC to 1D and 3D porous medium equation using deterministic particle method. The first row is 1D PME and the second row is 3D PME.

4.2 Keller-Segel equations

In this subsection we use twp deepSPoC algorithms(Algorithm 1 and Algorithm 3) to solve the Keller-Segel equation

$$\partial_t \mu = \nabla \cdot ((\nabla W * \mu) \mu) + \Delta \mu, \quad (x, t) \in \mathbb{R}^d \times (0, +\infty)$$

where

$$W(x) = \begin{cases} \frac{1}{2\pi} \ln(|x|) & \text{if } d = 2, \\ -\frac{C_d}{|x|^{d-2}} & \text{if } d \geq 3, \end{cases} \quad (34)$$

in which the constant $C_d = \frac{1}{d(d-2)\alpha_d}$. α_d denotes the volume of the unit ball in \mathbb{R}^d . It is a semilinear non-local PDE since it contains the convolution of distribution μ . The PDE can be associated with the following mean-field SDE:

$$dX_t = -(\nabla W * \mu_t)(X_t)dt + \sqrt{2}dB_t.$$

The convolution in this SDE represents the interaction between particles. The interaction kernel W is an attractive singular kernel. Specifically, the PoC result for the 2D case in (34) for this Keller-Segel chemotaxis model has been proven in [33]. When simulating SDEs as in (10) during the deepSPoC algorithm, we need to evaluate the convolution using Monte Carlo integration at each discrete time step t_m . In Algorithm 1, we use accept-reject sampling method to the density function approximated by the neural network $\rho_{FC,\theta}(t_m, \cdot)$ to generate $\{x_i\}_{i=1, \dots, N_g}$ independently. In Algorithm 3, we draw $\{x_i\}_{i=1, \dots, N_g}$ directly from KRnet $\rho_{NF,\theta}(t_m, \cdot)$. The independently generated x_i obeys the distribution $\mu_{t_m}^\theta$ with density function $\rho_{FC,\theta}(t_m, \cdot)$ or $\rho_{NF,\theta}(t_m, \cdot)$ and we estimate the convolution in the following way:

$$\nabla W * \mu_{t_m}^\theta(x) \approx \frac{1}{N_g} \sum_{i=1}^{N_g} \nabla W(x - x_i). \quad (35)$$

In this example, we do not know any solution of Keller-Segel equations that have an exact expression, so we cannot compare the solution we computed with the true solution directly. However, a property of the 2D Keller-Segel equation is that the second moment of the solution of the equation is linear [34] with respect to time and the slope can be explicitly expressed as $4(1 - \frac{1}{8\pi})$. Therefore we use this property to show the effectiveness of deepSPoC algorithm when solving 2D Keller-Segel equations, where $W(x) = 1/(2\pi)\ln(|x|)$. In particular, in each epoch, we record the second moment of the distribution at each discrete time (again using Monte Carlo method to estimate the second moment), then we calculate the slope of the second moment using least square method to see whether the change of the second moment according to time converges to straight line with the theoretical slope.

The first initial distribution we choose for our experiment is a 2D Gaussian distribution, which has the density function of $\rho_0(x_1, x_2) = \frac{1}{0.36\pi} \exp(-\frac{x_1^2 + x_2^2}{0.36})$. We also choose a mixed Gaussian distribution consists of two weighted Gaussian distributions as a relatively more complicated initial condition, in this case $\rho_0(x_1, x_2)$

$$\rho_0(x_1, x_2) = \frac{1}{3} \cdot \frac{1}{0.36\pi} \exp\left(-\frac{(x_1 + 1.5)^2 + x_2^2}{0.36}\right) + \frac{2}{3} \cdot \frac{1}{0.36\pi} \exp\left(-\frac{(x_1 - 1)^2 + x_2^2}{0.36}\right).$$

The N_g in (35) is set to 500. For both algorithms, we apply same parameters. Total time span is 0.2 and time discrete size is 0.01, number of training points N for each epoch is 2000, which is uniformly sampled from region $[-4, 4]^2$, the number of sampled particles K for each epoch is 2000. The initial learning rate of optimizer is 0.001 and it is decreased by a contraction factor $\gamma = 0.7$ for every $\Gamma = 500$ epochs. In Algorithm 1, the parameter ϵ for the mollifier is set to be 0.02. The evolution graph of the solution computed by Algorithm 1 after 8000 epochs at different time is shown in Fig. 10(a) 10(c), which is still the cut view with respect to the first spatial variable. The evolution of the second moment computed by Algorithm 1 with respect to epoch for two different initial distributions are shown in Fig. 10(b) 10(d) respectively. We can see that during the training process, the slopes of second moments gradually converge to the theoretical value. For Algorithm 3, we present same numerical results in Fig. 11(a), Fig. 11(b), Fig. 11(c) and Fig. 11(d). We observe that both algorithms can solve the problem with reasonable accuracy. However, in this example, Algorithm 1 outperforms Algorithm 3 (especially for mixed Gaussian distribution in domain $[-1, 0]$). One possible reason is the probability that particles run into interval $[-1, 0]$ is too low and therefore path data information is not enough for Algorithm 3 to generate an accurate solution here.

4.3 Curie-Weiss mean-field equations

This example is known as the Curie-Weiss mean-field equation. It is an expectation dependent mean-field SDE in the following form

$$dX_t = (-\beta(X_t^3 - X_t) + \beta K \mathbb{E} X_t) dt + dB_t,$$

where we set $\beta = 1$, $K = -0.1$. The equation has an explicit invariant measure and we show the asymptotic behavior of deepSPoC solution to the invariant measure in a relatively longer time. We use a PoC solution as reference solution and compare our result with it. The invariant measure has the following density (cf. [35])

$$p^*(x) = \frac{1}{C} \exp\left(-2\beta\left(\frac{x^4}{4} - \frac{x^2}{2}\right)\right),$$

where $C = \int_{\mathbb{R}} \exp\left(-2\beta\left(\frac{x^4}{4} - \frac{x^2}{2}\right)\right) dx$. The PoC solution is generated by 5 million particles and the deepSPoC solution is generated by 5000 training epochs with each epoch 1000 sampled particles. Therefore, we can consider

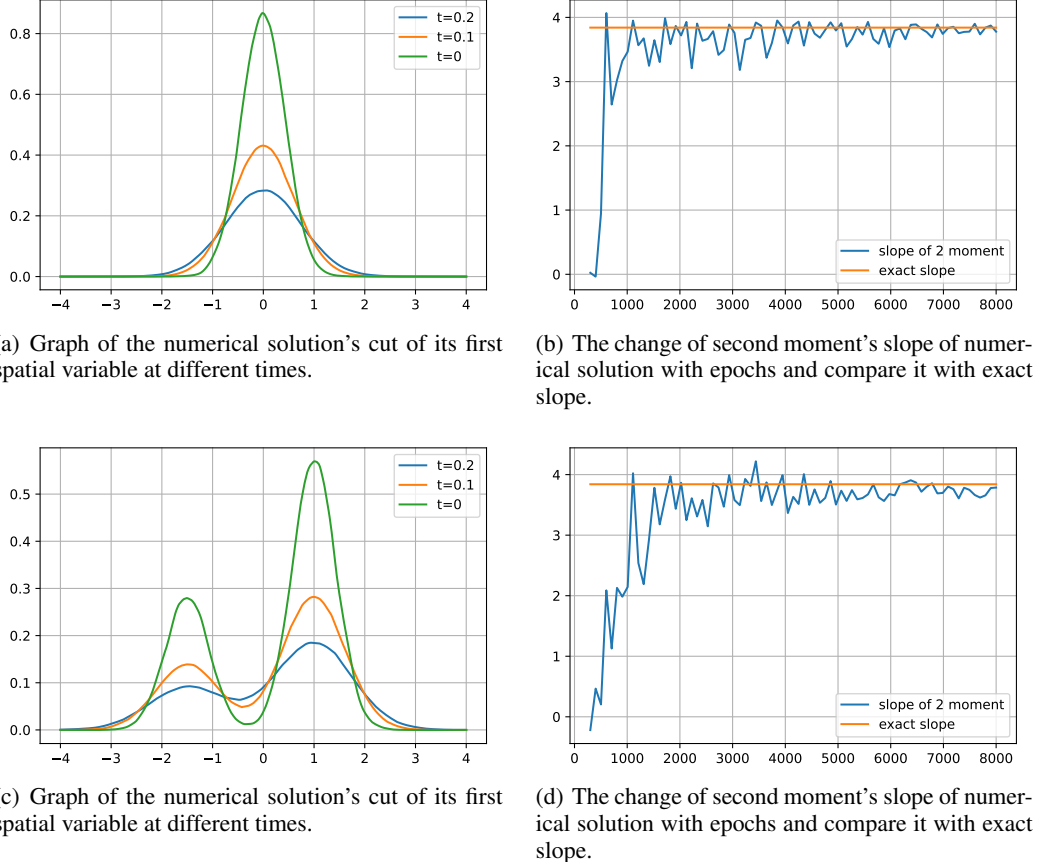


Figure 10: Result of 2D Keller-Segel equation for different initial distributions computed by deepSPoC with fully connected neural networks and loss function L_{sq} .

that the two solutions are generated by the same number of particles and we also use the same size of mollification for the two solutions. Specifically, the reference PoC solution which we show and compare with deepSPoC solution at time t is

$$\frac{1}{5000000} \sum_{i=1}^{5000000} \delta_{X_t^i} * f_\epsilon.$$

We choose the $\mathcal{N}(1, 1)$ as the initial distribution, which is a standard Gaussian distribution shifted one unit to the right. The time discretization size is 0.01 for both PoC and deepSPoC method (Algorithm 1 uniform version). We still use accept-reject sampling during deepSPoC to estimate the expectation of the neural network fitted density function at each discrete time point by sampling 100 particles each time. The number of training points N for each epoch is 1000 and it is sampled uniformly from a truncated region $\Omega_0 = [-3, 3]$. The initial learning rate is still 0.001 and is reduced to half every 500 epochs. The parameter ϵ for the Gaussian mollifier is 0.01. The comparison of the two solutions at $t = 2, 4, 6, 8, 10$ is shown in the first 5 figures in Fig. 12 and the last one is the invariant measure of this equation. We can see from the figure that the deepSPoC solution (the blue line) is almost the same as the PoC solution (the red dashes) and it can gradually converge to the invariant measure.

4.4 Fractional porous medium equations

The last example is solving the following fractional porous medium equation (FPME)

$$\partial_t \rho = -(-\Delta)^{\frac{\alpha}{2}} (|\rho|^{m-1} \rho)$$

where $m > 1$, $\alpha \in (0, 2)$ and $(-\Delta)^{\frac{\alpha}{2}}$ is the fractional Laplacian defined by

$$(-\Delta)^{\frac{\alpha}{2}} f(x) = C_{d,\alpha} \text{P.V.} \int_{\mathbb{R}^d} \frac{f(x) - f(y)}{|x - y|^{d+\alpha}} dy$$

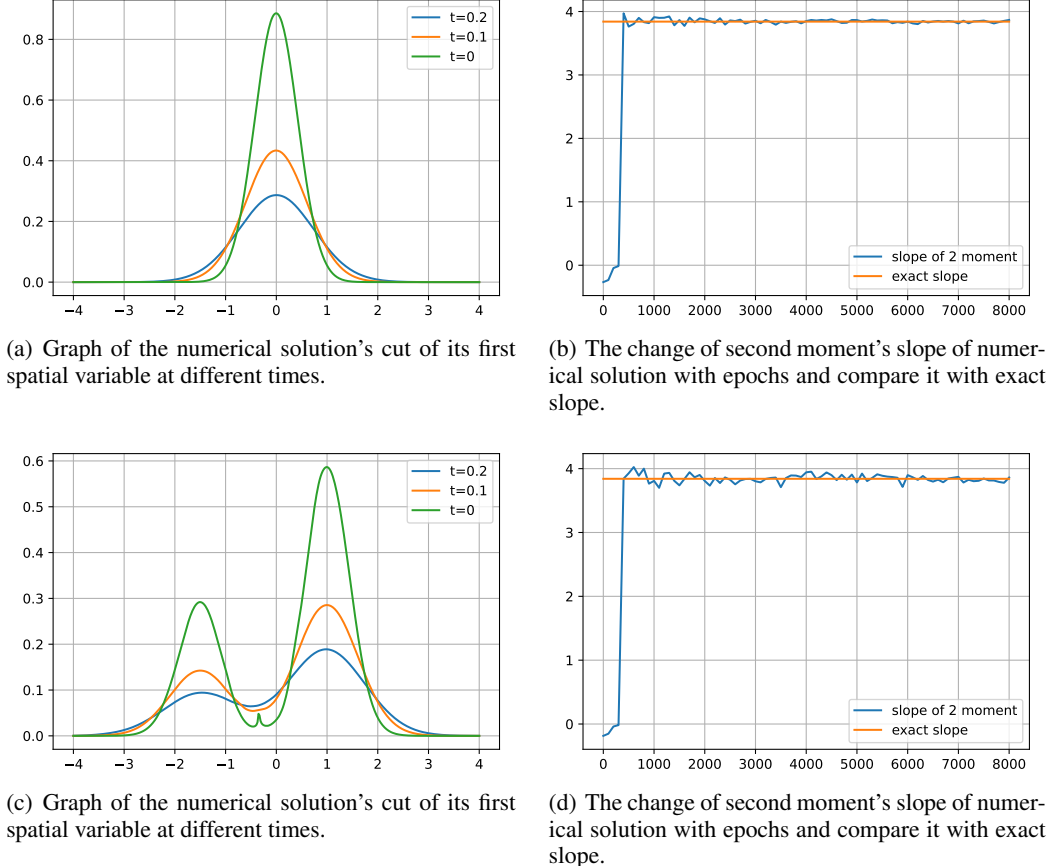


Figure 11: Result of 2D Keller-Segel equation for different initial distributions computed by deepSPoC with normalizing flows and loss function L_{path} .

where the normalization constant $C_{d,\alpha} = 2^{\alpha-1}\alpha\Gamma(\frac{d+\alpha}{2})/\pi^{N/2}\Gamma(1-\frac{\alpha}{2})$. It is a degenerate and non-local parabolic equation that appears naturally as the limiting equation of particle systems with jumps or long-range interactions. In [36], it is proved that the weak solution of the above FPME can be represented as the distributional density of the solution of the following distribution dependent SDE driven by α -stable process L_t^α

$$dX_t = \rho(t, X_{t-})^{\frac{m-1}{\alpha}} dL_t^\alpha.$$

In our experiment, we set $d = 1$, $\alpha = 1$ and $m = 2$. We compare our deepSPoC(Algorithm 1 uniform version) solution with a reference solution calculated by a finite difference method introduced in [37]. It should be pointed out that we can also apply deepSPoC to higher-dimensional FPMEs. However, from [37] we can only compute reference solutions of 1D FPMEs according to the method in this paper we need to expand the space dimension from d to $d + 1$ then apply finite difference method to the expanded equation, which makes the computational costs for solving FPMEs in two or more dimensions become too large. Therefore, we only compare the deepSPoC solution and the reference solution in the one-dimensional case of FPMEs.

The discrete time step for deepSPoC is 0.01 and the number of sample is $K = 2000$. The number of training points N is 2000 and they are uniformly sampled from the region $\Omega_0 = [-3, 3]$. Other settings are the same as the 1d PME experiment. We choose a normalized Barenblatt solution as our initial distribution such that we can observe the different behavior between FPME solution and PME solution more clearly. The result is shown in Fig 13, which consists of the images of deepSPoC solution after 5000 epochs (the green line) and the reference solution (with spatial step size 0.005 in the original and extend dimension, and time step size 0.005, the red dashes) at two different time points. We can see that the deepSPoC solution is close to the reference solution and it has infinite propagation speed and "long-tail" shape which is different from the case of PME.

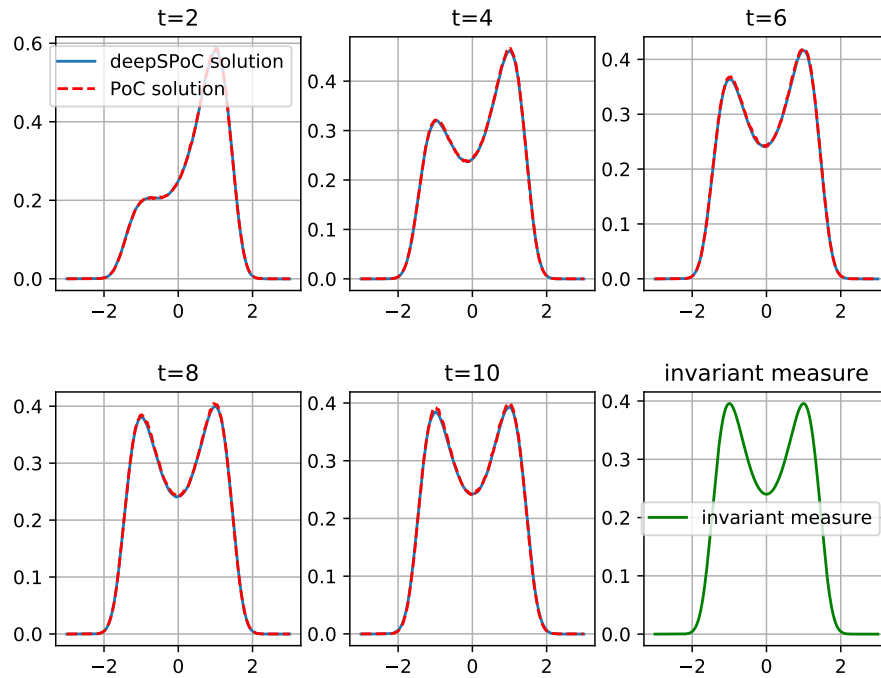


Figure 12: The figure of numerical solutions of CW equation at $t = 2, 4, 6, 8, 10$ and its invariant measure.

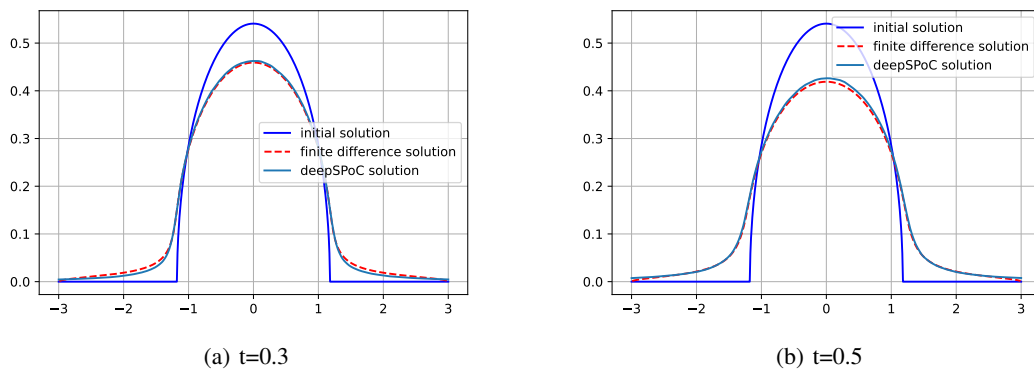


Figure 13: Results of 1D fractional porous medium equation for different time.

5 Conclusion

We propose an algorithm framework for solving nonlinear Fokker-Planck equations. Within this framework, we apply two different network architectures, fully connected and KRnet, and design multiple corresponding loss functions. The effectiveness of our algorithm is verified in different numerical examples. We have theoretically proven the convergence of the algorithm for approximating density functions using Fourier basis functions within this framework. We also analyze the theoretical posterior error estimation of the algorithm framework. At the same time, the experimental results show that for high-dimensional problems, the adaptive method we designed has played an important role in improving the accuracy and efficiency of the algorithm.

In the future, we hope to apply this algorithm framework to a wider range of equations, such as nonlinear Vlasov-Poisson-Fokker-Planck equations corresponding to second-order systems. We hope to conduct a more in-depth theoretical analysis of the algorithm framework in the future regarding the selection of network architecture and corresponding loss functions to further explain the effectiveness of the algorithm and improve its performance.

A Proofs for the results in Section 3

A.1 Proof of Proposition 3.2

From the integral form of the equation that $X_t^{i,n}$ satisfies, we have

$$\begin{aligned} \mathbb{E} \left(\sup_{0 \leq s \leq t} |X_s^{i,n}|^3 \right) &= \mathbb{E} \left(\sup_{0 \leq s \leq t} \left| X_0^{i,n} + \int_0^s b(r, X_r^{i,n}, \rho_{\theta_{n-1}^t}) dr + \int_0^s \sigma(r, X_r^{i,n}, \rho_{\theta_{n-1}^t}) dB_r^{i,n} \right|^3 \right) \\ &\leq 9\mathbb{E}(|X_0^{i,n}|^3) + 9\mathbb{E} \left(\sup_{0 \leq s \leq t} \left| \int_0^s b(r, X_r^{i,n}, \rho_{\theta_{n-1}^t}) dr \right|^3 \right) \\ &\quad + 9\mathbb{E} \left(\sup_{0 \leq s \leq t} \left| \int_0^s \sigma(r, X_r^{i,n}, \rho_{\theta_{n-1}^t}) dB_r^{i,n} \right|^3 \right). \end{aligned} \quad (36)$$

Using Hölder's inequality and assumption 3.1, we have

$$\begin{aligned} &\mathbb{E} \left(\sup_{0 \leq s \leq t} \left| \int_0^s b(r, X_r^{i,n}, \rho_{\theta_{n-1}^t}) dr \right|^3 \right) \\ &\leq T^2 \mathbb{E} \left(\int_0^t |b(r, X_r^{i,n}, \rho_{\theta_{n-1}^t})|^3 dr \right) \\ &\leq T^2 C^3 \mathbb{E} \left(\int_0^t (1 + X_r^{i,n} + \|\rho_{\theta_{n-1}^r}\|_1)^3 dr \right) \\ &\leq 9T^3 C^3 + 9T^2 C^3 \mathbb{E} \int_0^t |X_r^{i,n}|^3 dr + 9T^2 C^3 \mathbb{E} \int_0^t \|\rho_{\theta_{n-1}^r}\|_1^3 dr. \end{aligned} \quad (37)$$

Similarly, using BDG's inequality together assumption 3.1, we have

$$\begin{aligned} &\mathbb{E} \left(\sup_{0 \leq s \leq t} \left| \int_0^s \sigma(r, X_r^{i,n}, \rho_{\theta_{n-1}^t}) dB_r^{i,n} \right|^3 \right) \\ &\leq C_{BDG} \mathbb{E} \left(\int_0^t |\sigma(r, X_r^{i,n}, \rho_{\theta_{n-1}^r})|^3 dr \right) \\ &\leq 9TC_{BDG} C^3 + 9C_{BDG} C^3 \mathbb{E} \int_0^t |X_r^{i,n}|^3 dr + 9C_{BDG} C^3 \mathbb{E} \int_0^t \|\rho_{\theta_{n-1}^r}\|_1^3 dr. \end{aligned} \quad (38)$$

Recall that we have already had an explicit expression of $\rho_{\theta_{n-1}^r}$ according to (24) which is

$$\rho_{\theta_{n-1}^r} = \sum_{l=0}^{n-1} \beta_l P_N \left(\frac{1}{K} \sum_{i=1}^K \delta_{\tilde{X}_r^{i,l}}^\epsilon \right) = P_N \left(\sum_{l=0}^{n-1} \frac{\beta_l}{K} \sum_{i=1}^K \delta_{\tilde{X}_r^{i,l}}^\epsilon \right),$$

where $\beta_l = (1-2\alpha_{n-1})(1-2\alpha_{n-2}) \dots (1-2\alpha_{l+1})2\alpha_l$ is the weight of l -th batch of particles that satisfies $\sum_{l=0}^{n-1} \beta_l = 1$. Then by (26) and the property of Wasserstein distance, we have

$$\begin{aligned} \|\rho_{\theta_{n-1}^r}\|_1 &\leq \left\| \sum_{l=0}^{n-1} \frac{\beta_l}{K} \sum_{i=1}^K \delta_{\tilde{X}_r^{i,l}}^\epsilon \right\|_1 + \epsilon \\ &\leq \left\| \sum_{l=0}^{n-1} \frac{\beta_l}{K} \sum_{i=1}^K \delta_{\tilde{X}_r^{i,l}} \right\|_1 + 2\epsilon \\ &\leq \sum_{l=0}^{n-1} \frac{\beta_l}{K} \sum_{i=1}^K |X_r^{i,l}| + 2\epsilon, \end{aligned}$$

the third inequality uses the definition of $\|\cdot\|_1$ and the truncated particle. Furthermore, by Jensen's inequality and the convexity of function $|x|^3$, we have

$$\begin{aligned} \|\rho_{\theta_{n-1}^r}\|_1^3 &\leq \left(\sum_{l=0}^{n-1} \frac{\beta_l}{K} \sum_{i=1}^K |X_r^{i,l}| + 2\epsilon \right)^3 \\ &\leq 4 \left(\sum_{l=0}^{n-1} \frac{\beta_l}{K} \sum_{i=1}^K |X_r^{i,l}| \right)^3 + 4(2\epsilon)^3 \\ &\leq 4 \left(\sum_{l=0}^{n-1} \frac{\beta_l}{K} \sum_{i=1}^K |X_r^{i,l}|^3 \right) + 4(2\epsilon)^3 \end{aligned} \tag{39}$$

Put the estimation (39) into (37) and (38), and comeback to (36), we will find that there exists a constant C_1 depending only on C, T, C_{BDG} and μ_0 such that

$$\begin{aligned} \mathbb{E} \left(\sup_{0 \leq s \leq t} |X_s^{i,n}|^3 \right) &\leq C_1 \left(1 + \int_0^t \mathbb{E} |X_r^{i,n}|^3 dr + \sum_{l=0}^{n-1} \frac{\beta_l}{K} \sum_{i=1}^K \int_0^t \mathbb{E} |X_r^{i,l}|^3 dr \right) \\ &\leq C_1 \left(1 + \int_0^t \mathbb{E} \sup_{0 \leq s \leq r} |X_s^{i,n}|^3 dr + \sum_{l=0}^{n-1} \frac{\beta_l}{K} \sum_{i=1}^K \int_0^t \mathbb{E} \sup_{0 \leq s \leq r} |X_s^{i,l}|^3 dr \right). \end{aligned} \tag{40}$$

Let $C_2 = \max\{\|\mu_0\|_3^3, 2C_1 e^{C_1 T}\}$, $C_3 = 2C_1 e^{C_1 T}$, we now argue by induction on n that $\mathbb{E} (\sup_{0 \leq s \leq t} |X_s^{i,n}|^3) \leq C_2 e^{C_3 t}$, according the definition of C_2 , it is true when $n = 0$. If $n \geq 1$, then by (40), we obtain

$$\mathbb{E} \left(\sup_{0 \leq s \leq t} |X_s^{i,n}|^3 \right) \leq C_1 \left(1 + \int_0^t \mathbb{E} \sup_{0 \leq s \leq r} |X_s^{i,n}|^3 dr + \frac{C_2}{C_3} (e^{C_2 t} - 1) \right),$$

by Grownwall's inequality and the definition of C_2, C_3 , we have

$$\begin{aligned} \mathbb{E} \left(\sup_{0 \leq s \leq T} |X_s^{i,n}|^3 \right) &\leq e^{C_1 t} (C_1 + \frac{C_1 C_2}{C_3} (e^{C_3 t} - 1)) \\ &\leq C_1 e^{C_1 t} + \frac{1}{2} C_2 e^{C_3 t} \leq C_2 e^{C_3 t}. \end{aligned}$$

Let $C_0 = C_2 e^{C_3 T}$, then we have proved the first argument of this proposition, and the second one follows easily from

$$\mathbb{E} \left((\sup_{0 \leq s \leq T} |X_s^{i,n}|^2) \cdot 1_{\{\sup_{0 \leq s \leq T} |X_s^{i,n}| \geq L_0\}} \right) \leq \mathbb{E} \left(\sup_{0 \leq s \leq T} |X_s^{i,n}|^3 \right) / L_0.$$

The proof is complete.

A.2 Proof of Theorem 3.3

Recall that we assume in our main convergence theorem that the learning rate α_n is chosen to make all the particles have the same weight. In fact, no matter what weights of particles we choose, the convergence speed will always come from a sequence of recursive Grownwall-like inequalities, the next lemma is about to tackle such inequalities of the equal weights case which will occur in the proof of our main theorem.

Lemma A.1. *For a sequence of recursive inequalities*

$$\frac{dx_i(t)}{dt} \leq Cx_i(t) + \frac{L}{i} \sum_{j=0}^{i-1} x_j(t) + M\tau_i,$$

where $t \in [0, T]$, $x_i(0) = 0$ ($i \geq 0$) and C, L, M are constants, and τ_i satisfies that there exists a constant C_0 such that for any $i \geq 0$,

$$\frac{\tau_0 + \tau_1 + \cdots + \tau_{i-1}}{i} \leq C_0\tau_i,$$

then we can find a constant \bar{C} independent of i such that for any $i \geq 0$ and $t \in [0, T]$,

$$x_i(t) \leq \bar{C}\tau_i.$$

Proof. we prove the following argument by induction

$$x_i(t) \leq C_1 e^{C_2 t} \tau_i, t \in [0, T],$$

where $C_2 = e^{CT} LC_0$. C_1 is chosen big enough to satisfies $C_1 > e^{CT} MT$ and to make the above argument is true for $i = 0$ at the same time. Then for $i \geq 1$, suppose the argument is true for $j \leq i$, we have

$$\begin{aligned} \frac{dx_i(t)}{dt} &\leq Cx_i(t) + \frac{L}{i} \sum_{j=0}^{i-1} C_1 e^{C_2 \tau_j} + M\tau_i \\ &\leq Cx_i(t) + LC_1 e^{C_2 t} C_0 \tau_i + M\tau_i \\ &\leq Cx_i(t) + (LC_0 C_1 e^{C_2 t} + M)\tau_i, \end{aligned}$$

By Grownwall's inequality,

$$\begin{aligned} x_i(t) &\leq e^{CT} \int_0^t (LC_0 C_1 e^{C_2 \tau} + M) d\tau \\ &= \left((e^{CT} LC_0) \frac{C_1}{C_2} (e^{C_2 t} - 1) + e^{CT} Mt \right) \tau_i \\ &= (C_1 (e^{C_2 t} - 1) + e^{CT} Mt) \tau_i \\ &\leq C_1 e^{C_2 t} \tau_i. \end{aligned}$$

So the argument is true, then we finish the proof by setting $\bar{C} = C_1 e^{C_2 T}$. \square

Now we give the proof of Theorem 3.3.

Proof of Theorem 3.3. Using synchronous coupling method, we introduce particles $Y_t^{i,n}$ to satisfy the following mean field limit equation

$$\begin{cases} dY_t^{i,n} = b(t, Y_t^{i,n}, \mu_t) dt + \sigma(t, Y_t^{i,n}, \mu_t) dB_t^{i,n}, & i = 1, \dots, K \\ Y_0^{i,n} = X_0^{i,n}, \end{cases}$$

where μ_t is the distribution of $Y_t^{i,n}$, notice that $Y_t^{i,n}$ are all i.i.d. random variables. Denote $Z_t^{i,n} := X_t^{i,n} - Y_t^{i,n}$, we have $Z_0^{i,n} = 0$ and

$$\begin{aligned} d|Z_t^{i,n}|^2 &= 2Z_t^{i,n} \cdot \left(b(t, X_t^{i,n}, \rho_{\theta_{n-1}^t}) - b(t, Y_t^{i,n}, \mu_t) \right) dt \\ &\quad + 2Z_t^{i,n} \cdot \left(\sigma(t, X_t^{i,n}, \rho_{\theta_{n-1}^t}) - \sigma(t, Y_t^{i,n}, \mu_t) \right) dB_t^{i,n} \\ &\quad + \left\| \sigma(t, X_t^{i,n}, \rho_{\theta_{n-1}^t}) - \sigma(t, Y_t^{i,n}, \mu_t) \right\|^2 dt. \end{aligned}$$

Take expectation from both side and use assumption 3.1, we obtain

$$\begin{aligned}
 d\mathbb{E}|Z_t^{i,n}|^2 &= 2\mathbb{E}\left(Z_t^{i,n} \cdot \left(b\left(t, X_t^{i,n}, \rho_{\theta_{n-1}^t}\right) - b\left(t, Y_t^{i,n}, \mu_t\right)\right)\right) dt \\
 &\quad + \mathbb{E}||\sigma(t, X_t^{i,n}, \rho_{\theta_{n-1}^t}) - \sigma(t, Y_t^{i,n}, \mu_t)||^2 dt \\
 &\leq \mathbb{E}|Z_t^{i,n}|^2 dt + \mathbb{E}|b(t, X_t^{i,n}, \rho_{\theta_{n-1}^t}) - b(t, Y_t^{i,n}, \mu_t)|^2 dt \\
 &\quad + \mathbb{E}||\sigma(t, X_t^{i,n}, \rho_{\theta_{n-1}^t}) - \sigma(t, Y_t^{i,n}, \mu_t)||^2 dt \\
 &\leq (1 + 4C^2)\mathbb{E}|Z_t^{i,n}|^2 dt + 4C^2\mathbb{E}W_1^2(\rho_{\theta_{n-1}^t}, \mu_t)dt.
 \end{aligned}$$

We now carefully analyze the latter term, since $\beta_l = \frac{1}{n}$, then

$$\begin{aligned}
 \mathbb{E}W_1^2(\rho_{\theta_{n-1}^t}, \mu_t) &= \mathbb{E}W_1^2\left(P_N\left(\frac{1}{Kn} \sum_{l=0}^{n-1} \sum_{i=1}^K \delta_{\tilde{X}_r^{i,l}}^\epsilon\right), \mu_t\right) \\
 &\leq 2\mathbb{E}W_1^2\left(P_N\left(\frac{1}{Kn} \sum_{l=1}^{n-1} \sum_{i=1}^K \delta_{\tilde{X}_r^{i,l}}^\epsilon\right), \frac{1}{Kn} \sum_{l=0}^{n-1} \sum_{i=1}^K \delta_{Y_r^{i,l}}\right) + 2\mathbb{E}W_1^2\left(\frac{1}{Kn} \sum_{l=0}^{n-1} \sum_{i=1}^K \delta_{Y_r^{i,l}}, \mu_t\right), \tag{41}
 \end{aligned}$$

where

$$\begin{aligned}
 &\mathbb{E}W_1^2\left(P_N\left(\frac{1}{Kn} \sum_{l=1}^{n-1} \sum_{i=1}^K \delta_{\tilde{X}_r^{i,l}}^\epsilon\right), \frac{1}{Kn} \sum_{l=0}^{n-1} \sum_{i=1}^K \delta_{Y_r^{i,l}}\right) \\
 &\leq 2\mathbb{E}W_1^2\left(\frac{1}{Kn} \sum_{l=1}^{n-1} \sum_{i=1}^K \delta_{\tilde{X}_r^{i,l}}, \frac{1}{Kn} \sum_{l=0}^{n-1} \sum_{i=1}^K \delta_{Y_r^{i,l}}\right) + 2(2\epsilon)^2 \\
 &\leq 2\mathbb{E}\left(\frac{1}{Kn} \sum_{l=0}^{n-1} \sum_{i=1}^K |\tilde{X}_r^{i,l} - Y_r^{i,l}|\right)^2 + 8\epsilon^2 \\
 &\leq 2\mathbb{E}\left(\frac{1}{Kn} \sum_{l=0}^{n-1} \sum_{i=1}^K |\tilde{X}_r^{i,l} - Y_r^{i,l}|^2\right) + 8\epsilon^2 \\
 &\leq 2\mathbb{E}\left(\frac{1}{Kn} \sum_{l=0}^{n-1} \sum_{i=1}^K |X_r^{i,l} - Y_r^{i,l}|^2\right) + 10\epsilon^2 \\
 &= 2\mathbb{E}\left(\frac{1}{Kn} \sum_{l=0}^{n-1} \sum_{i=1}^K |Z_r^{i,l}|^2\right) + 10\epsilon^2,
 \end{aligned}$$

the last inequality comes from (27). Another term of (41) is about the convergence of empirical measures in the Wasserstein distance, and we refer to the lemma 3.3 in [15] to get the following estimate

$$\mathbb{E}W_1^2\left(\frac{1}{Kn} \sum_{l=0}^{n-1} \sum_{i=1}^K \delta_{Y_r^{i,l}}, \mu_t\right) \leq C\left(\frac{1}{Kn}\right)^{\frac{1}{1+d/2}},$$

where C is a constant independent of n and K . Then we obtain that there exists a constant C_0 such that

$$\frac{d\mathbb{E}|Z_t^{i,n}|^2}{dt} \leq C_0 \left(\mathbb{E}|Z_t^{i,n}|^2 + \frac{1}{Kn} \sum_{l=0}^{n-1} \sum_{i=1}^K \mathbb{E}|Z_r^{i,l}|^2 + \epsilon^2 + \frac{1}{(Kn)^{\frac{1}{1+d/2}}} \right).$$

Let $\tau_l = \epsilon^2 + \frac{1}{(Kl)^{\frac{1}{1+d/2}}}$, it is easy to verify that τ_l satisfy the condition of Lemma A.1, then by this lemma we can obtain that

$$\mathbb{E}|Z_t^{i,l}|^2 \leq \bar{C} \left(\epsilon^2 + \frac{1}{(Kl)^{\frac{1}{1+d/2}}} \right),$$

where \bar{C} is the constant from this lemma. Then we put the above estimation into (41)

$$\begin{aligned}
 \mathbb{E}W_1^2(\rho_{\theta_{n-1}^t}, \mu_t) &\leq 2\mathbb{E}\left(\frac{1}{Kn} \sum_{l=0}^{n-1} \sum_{i=1}^K |Z_r^{i,l}|^2\right) + 10\epsilon^2 + C\left(\frac{1}{Kn}\right)^{\frac{1}{1+d/2}} \\
 &\leq C_1(\epsilon^2 + (Kn)^{\frac{1}{1+d/2}}).
 \end{aligned}$$

The proof is complete. \square

A.3 Proof of Proposition 3.5

Again using synchronous coupling method, for $\mu, \nu \in \mathcal{P}_{2,\infty}([0, T])$, we introduce the following two Markovian SDEs:

$$\begin{aligned} dX_t &= b(t, X_t, \mu_t)dt + \sigma(t, X_t, \mu_t)dB_t, \\ dY_t &= b(t, Y_t, \nu_t)dt + \sigma(t, Y_t, \nu_t)dB_t, \end{aligned}$$

where $X_0 = Y_0 \sim \bar{\mu}$. Then we have

$$\begin{aligned} \mathbb{E}|X_t - Y_t|^2 &\leq 2\mathbb{E} \left| \int_0^t b(s, X_s, \mu_s) - b(s, Y_s, \nu_s) ds \right|^2 + 2\mathbb{E} \left| \int_0^t \sigma(s, X_s, \mu_s) - \sigma(s, Y_s, \nu_s) dW_s \right|^2 \\ &\leq 2t\mathbb{E} \int_0^t |b(s, X_s, \mu_s) - b(s, Y_s, \nu_s)|^2 ds + 2\mathbb{E} \int_0^t \|\sigma(s, X_s, \mu_s) - \sigma(s, Y_s, \nu_s)\|^2 ds \\ &\leq 2(T+1)C^2 \left(\mathbb{E} \int_0^t |X_s - Y_s|^2 ds + \mathbb{E} \int_0^t W_2^2(\mu_s, \nu_s) ds \right). \end{aligned}$$

Multiplying both sides by $e^{-\alpha t}$ and integrating from 0 to T , we obtain

$$\begin{aligned} &\int_0^T e^{-\alpha t} \mathbb{E}|X_t - Y_t|^2 dt \\ &\leq 2(T+1)C^2 \int_0^T e^{-\alpha t} \left(\mathbb{E} \int_0^t |X_s - Y_s|^2 ds \right) dt + 2(T+1)C^2 \int_0^T e^{-\alpha t} \left(\int_0^t W_2^2(\mu_s, \nu_s) ds \right) dt, \end{aligned}$$

By exchanging the order of integration, we obtain

$$\begin{aligned} &\int_0^T e^{-\alpha t} \left(\mathbb{E} \int_0^t |X_s - Y_s|^2 ds \right) dt \\ &= \mathbb{E} \int_0^T \int_0^t e^{-\alpha t} |X_s - Y_s|^2 ds dt \\ &= \mathbb{E} \int_0^T \int_s^T e^{-\alpha t} |X_s - Y_s|^2 dt ds \\ &= \mathbb{E} \int_0^T \int_s^T e^{-\alpha(t-s)} e^{-\alpha s} |X_s - Y_s|^2 dt ds \\ &\leq \frac{1}{\alpha} \int_0^T e^{-\alpha s} \mathbb{E}|X_s - Y_s|^2 ds. \end{aligned}$$

Similarly we can obtain

$$\int_0^T e^{-\alpha t} \left(\int_0^t W_2^2(\mu_s, \nu_s) ds \right) dt \leq \frac{1}{\alpha} \int_0^T e^{-\alpha s} W_2^2(\mu_s, \nu_s) ds.$$

Then we have

$$\int_0^T e^{-\alpha t} \mathbb{E}|X_t - Y_t|^2 dt \leq \frac{2(T+1)C^2}{\alpha} \int_0^T e^{-\alpha t} \mathbb{E}|X_t - Y_t|^2 dt + \frac{2(T+1)C^2}{\alpha} \int_0^T e^{-\alpha t} W_2^2(\mu_t, \nu_t) dt,$$

use the property that $W_2^2(\text{Law}(X_t), \text{Law}(Y_t)) \leq \mathbb{E}|Y_t - X_t|^2$ and recall the definition of Φ we get

$$\left(1 - \frac{2(T+1)C^2}{\alpha} \right) \int_0^T e^{-\alpha t} W_2^2(\Phi(\mu.)_t, \Phi(\nu.)_t) dt \leq \frac{2(T+1)C^2}{\alpha} \int_0^T e^{-\alpha t} W_2^2(\mu_t, \nu_t) dt.$$

The conclusion we aim to prove can be easily obtained from the above inequality.

References

- [1] Louis-Pierre Chaintron and Antoine Diez. Propagation of chaos: a review of models, methods and applications. ii. applications. *arXiv preprint arXiv:2106.14812*, 2021.
- [2] Henry P McKean. Propagation of chaos for a class of non-linear parabolic equations. *Stochastic Differential Equations (Lecture Series in Differential Equations, Session 7, Catholic Univ., 1967)*, pages 41–57, 1967.
- [3] Alain-Sol Sznitman. Topics in propagation of chaos. *Lecture notes in mathematics*, pages 165–251, 1991.
- [4] José Antonio Carrillo, Katy Craig, and Francesco S Patacchini. A blob method for diffusion. *Calculus of Variations and Partial Differential Equations*, 58:1–53, 2019.
- [5] José A Carrillo, Helene Ranetbauer, and Marie-Therese Wolfram. Numerical simulation of nonlinear continuity equations by evolving diffeomorphisms. *Journal of Computational Physics*, 327:186–202, 2016.
- [6] Mireille Bossy and Denis Talay. A stochastic particle method for the McKean-Vlasov and the Burgers equation. *Mathematics of computation*, 66(217):157–192, 1997.
- [7] Anthony Le Cavil, Nadia Oudjane, and Francesco Russo. Particle system algorithm and chaos propagation related to non-conservative McKean type stochastic differential equations. *Stochastics and Partial Differential Equations: Analysis and Computations*, 5:1–37, 2017.
- [8] Nadia Belaribi, François Cuvelier, and Francesco Russo. A probabilistic algorithm approximating solutions of a singular PDE of porous media type. *Monte Carlo Methods and Applications*, 17(4):317–369, 2011.
- [9] Nadia Belaribi, François Cuvelier, and Francesco Russo. Probabilistic and deterministic algorithms for space multidimensional irregular porous media equation. *Stochastic Partial Differential Equations: Analysis and Computations*, 1(1):3–62, 2013.
- [10] Shi Jin, Lei Li, and Jian-Guo Liu. Random batch methods (rbm) for interacting particle systems. *Journal of Computational Physics*, 400:108877, 2020.
- [11] Maziar Raissi, Paris Perdikaris, and George E Karniadakis. Physics-informed neural networks: A deep learning framework for solving forward and inverse problems involving nonlinear partial differential equations. *Journal of Computational Physics*, 378:686–707, 2019.
- [12] Weinan E and Bing Yu. The deep Ritz method: a deep learning-based numerical algorithm for solving variational problems. *Communications in Mathematics and Statistics*, 6(1):1–12, 2018.
- [13] Yaohua Zang, Gang Bao, Xiaojing Ye, and Haomin Zhou. Weak adversarial networks for high-dimensional partial differential equations. *Journal of Computational Physics*, 411:109409, 2020.
- [14] Jiequn Han, Arnulf Jentzen, and Weinan E. Solving high-dimensional partial differential equations using deep learning. *Proceedings of the National Academy of Sciences*, 115(34):8505–8510, 2018.
- [15] Kai Du, Yifan Jiang, and Xiaochen Li. Sequential propagation of chaos. *arXiv preprint arXiv:2301.09913*, 2023.
- [16] David Applebaum. *Lévy processes and stochastic calculus*. Cambridge university press, 2009.
- [17] Mitia Duerinckx and Sylvia Serfaty. Mean field limit for Coulomb-type flows. *Duke Mathematical Journal*, 169(15):2887–2935, 2020.
- [18] Pierre-Emmanuel Jabin and Zhenfu Wang. Quantitative estimates of propagation of chaos for stochastic systems with $w^{-1,\infty}$ kernels. *Inventiones mathematicae*, 214:523–591, 2018.
- [19] Louis-Pierre Chaintron and Antoine Diez. Propagation of chaos: a review of models, methods and applications. i. models and methods. *arXiv preprint arXiv:2203.00446*, 2022.
- [20] Benjamin Jourdain and Sylvie Méléard. Propagation of chaos and fluctuations for a moderate model with smooth initial data. In *Annales de l’Institut Henri Poincaré (B) Probability and Statistics*, volume 34, pages 727–766. Elsevier, 1998.
- [21] Philip Protter and Denis Talay. The Euler scheme for Lévy driven stochastic differential equations. *The Annals of Probability*, pages 393–423, 1997.
- [22] Kejun Tang, Xiaoliang Wan, and Qifeng Liao. Adaptive deep density approximation for Fokker-Planck equations. *Journal of Computational Physics*, 457:111080, 2022.
- [23] Xiaodong Feng, Li Zeng, and Tao Zhou. Solving time dependent Fokker-Planck equations via temporal normalizing flow. *arXiv preprint arXiv:2112.14012*, 2021.
- [24] Danilo Rezende and Shakir Mohamed. Variational inference with normalizing flows. In *International conference on machine learning*, pages 1530–1538. PMLR, 2015.

[25] George Papamakarios, Eric Nalisnick, Danilo Jimenez Rezende, Shakir Mohamed, and Balaji Lakshminarayanan. Normalizing flows for probabilistic modeling and inference. *Journal of Machine Learning Research*, 22(57):1–64, 2021.

[26] Keju Tang, Xiaoliang Wan, and Qifeng Liao. Deep density estimation via invertible block-triangular mapping. *Theoretical and Applied Mechanics Letters*, 10(3):143–148, 2020.

[27] Yubin Lu, Romit Maulik, Ting Gao, Felix Dietrich, Ioannis G Kevrekidis, and Jinqiao Duan. Learning the temporal evolution of multivariate densities via normalizing flows. *Chaos: An Interdisciplinary Journal of Nonlinear Science*, 32(3), 2022.

[28] John C Mason. Near-best multivariate approximation by Fourier series, Chebyshev series and Chebyshev interpolation. *Journal of Approximation Theory*, 28(4):349–358, 1980.

[29] Feng-Yu Wang. Distribution dependent SDEs for Landau type equations. *Stochastic Processes and their Applications*, 128(2):595–621, 2018.

[30] Siddhartha Mishra and Roberto Molinaro. Estimates on the generalization error of physics-informed neural networks for approximating a class of inverse problems for PDEs. *IMA Journal of Numerical Analysis*, 42(2):981–1022, 2022.

[31] Siddhartha Mishra and Roberto Molinaro. Estimates on the generalization error of physics-informed neural networks for approximating PDEs. *IMA Journal of Numerical Analysis*, 43(1):1–43, 2023.

[32] Birgit Hillebrecht and Benjamin Unger. Certified machine learning: A posteriori error estimation for physics-informed neural networks. In *2022 International Joint Conference on Neural Networks (IJCNN)*, pages 1–8. IEEE, 2022.

[33] Didier Bresch, Pierre-Emmanuel Jabin, and Zhenfu Wang. On mean-field limits and quantitative estimates with a large class of singular kernels: Application to the Patlak–Keller–Segel model. *Comptes Rendus Mathematique*, 357(9):708–720, 2019.

[34] Giani Egaña Fernández and Stéphane Mischler. Uniqueness and long time asymptotic for the Keller–Segel equation: the parabolic–elliptic case. *Archive for Rational Mechanics and Analysis*, 220:1159–1194, 2016.

[35] Wenjing Cao and Kai Du. Empirical approximation to invariant measures of non-degenerate McKean–Vlasov dynamics. *arXiv preprint arXiv:2310.19302*, 2023.

[36] Michael Röckner, Longjie Xie, and Xicheng Zhang. Superposition principle for non-local Fokker–Planck–Kolmogorov operators. *Probability Theory and Related Fields*, 178(3):699–733, 2020.

[37] Félix del Teso. Finite difference method for a fractional porous medium equation. *Calcolo*, 51:615–638, 2014.